BRNO UNIVERSITY OF TECHNOLOGY
VYSOKÉ UČENÍ TECHNICKÉ V BRNĚ

FACULTY OF INFORMATION TECHNOLOGY
FAKULTA INFORMAČNÍCH TECHNOLOGIÍ

DEPARTMENT OF COMPUTER GRAPHICS AND MULTIMEDIA
ÚSTAV POČÍTAČOVÉ GRAFIKY A MULTIMÉDIÍ

MEASURING THE THICKNESS OF MATERIAL LAYERS REMOVED FROM A SAMPLE IN AN ELECTRON MICROSCOPE

MĚŘENÍ TLOUŠŤKY VRSTEV ODPRÁŠENÉHO MATERIÁLU ZE VZORKU V ELEKTRONOVÉM MIKROSKOPU

MASTER'S THESIS
DIPLOMOVÁ PRÁCE

AUTHOR **Bc. JIŘÍ KUTÁLEK**
AUTOR PRÁCE

SUPERVISOR **doc. Ing. MARTIN ČADÍK, Ph.D.**
VEDOUCÍ PRÁCE

BRNO 2023

BRNO UNIVERSITY OF TECHNOLOGY
FACULTY OF INFORMATION TECHNOLOGY

Master's Thesis Assignment

148415

Institut: Department of Computer Graphics and Multimedia (UPGM)
Student: **Kutálek Jiří, Bc.**
Programme: Information Technology and Artificial Intelligence
Specialization: Computer Vision
Title: **Measuring the Thickness of Material Layers Removed from a Sample in an Electron Microscope**
Category: Image Processing
Academic year: 2022/23

Assignment:

1. Get the basic knowledge of electron miscroscopy and the electron miscroscopy image characteristics.
2. Familiarize yourself with existing methods for measurement of the thickness of removed material layers.
3. Propose new methods improving the existing ones.
4. Experiment with the proposed methods and evaluate their precision and accuracy.
5. Discuss the results and applicability of the methods.

Literature:

- GOLDSTEIN, Joseph I., et al. *Scanning electron microscopy and X-ray microanalysis*. Springer, 2017.
- JONES, H. G.; MINGARD, K. P.; COX, D. C. Investigation of slice thickness and shape milled by a focused ion beam for three-dimensional reconstruction of microstructures. *Ultramicroscopy*, 2014, 139: 20-28.

Requirements for the semestral defence:
Items 1-3.

Detailed formal requirements can be found at https://www.fit.vut.cz/study/theses/

Supervisor: **Čadík Martin, doc. Ing., Ph.D.**
Consultant: Ing. Bronislav Přibyl, Ph.D.
Head of Department: Černocký Jan, prof. Dr. Ing.
Beginning of work: 1.11.2022
Submission deadline: 17.5.2023
Approval date: 8.12.2022

Abstract
The motivation for this thesis arises from the aim of the Thermo Fisher Scientific company to develop a method for the measurement of thickness of material layers removed from a sample in an electron microscope. The primary goal of this work is to propose a more effective measurement method, from a practical point of view, compared to the existing ones. Besides, the secondary goal is finding a way to obtain a ground truth for the measurement, to be able to evaluate the proposed solution. This thesis introduces two new measurement methods, based on detecting a sample edge from images, and proposes an approach for obtaining the ground truth, lying in carving tiny circular features into the sample surface and detecting and counting their numbers in acquired images. I created three different datasets of images for evaluating the performance of the methods. The experimental results show that one of the proposed methods, the Top-Down FIB, measures consistent values, which are close to the expected average and performs slightly better than the state-of-the-art method, when compared to the ground truth. Moreover, the algorithm counting the circular features in image appears to be usable for obtaining the ground truth, as it produces more stable results than a ground truth created by manually annotating the data.

Abstrakt
Motivace pro tuto práci vyvstává ze zájmu firmy Thermo Fisher Scientific o vyvinutí metody pro měření tloušťky vrstev odprášeného materiálu ze vzorku v elektronovém mikroskopu. Hlavním cílem práce je navržení meřicí metody, jež bude z praktického hlediska efektivnější než metody stávající. Mimo to, druhotným cílem je nalezení způsobu pro získání ground truth pro měření, která by umožnila navrženou metodu vyhodnotit. Tato práce představuje dvě nové meřicí metody detekující pozici hrany vzorku v obraze a způsob pro získání ground truth, spočívající ve vypálení drobných jamek (teček) do povrchu vzorku a následné detekce a počítání teček v obrázcích vzorku. Pro účely vyhodnocení všech metod jsem nasbíral tři sady obrázků. Výsledky experimentů ukazují, že jedna z navržených metod, Top-Down FIB, měří konzistentní hodnoty blízké očekávanému průměru a z porovnání vůču ground truth vychází o něco lépe, než state-of-the-art metoda. Navíc, algortimus počítající tečky v obraze se ukazál býti použitelnou metodou pro získání ground truth, neboť dosáhl stabilnějších výsledků, než alternativní ground truth vygenerovaná manuální anotací dat.

Keywords
Dual-beam Scanning Electron Microscope, Slice And View Approach, Slice Thickness Measurement, Cut-face edge detection, Referential dot pattern

Klíčová slova
Skenovací elektronový mikroskop “dual-beam”, Slice And View přístup, Měření tloušťky vrstev odprášeného materiálu, Detekce hrany cut-face, Referenční tečkovaný vzor

Reference
KUTÁLEK, Jiří. *Measuring the thickness of material layers removed from a sample in an electron microscope.* Brno, 2023. Master’s thesis. Brno University of Technology, Faculty of Information Technology. Supervisor doc. Ing. Martin Čadík, Ph.D.

Rozšířený abstrakt

Motivace Motivace pro tuto práci vyvstává ze zájmu firmy Thermo Fisher Scientific o vyvinutí metody schopné změřit tloušťku vrstev materiálu odprášeného ze vzorku v elektronovém mikroskopu, jež by byla z uživatelského pohledu praktičtější, než metody existující. Bohužel, neexistuje žádný způsob, jak porovnat metody existující s těmi navrženými, či jak vyhodnotit jejich přesnost, neboť neexistuje žádná ground truth (skutečná, referenční hodnota).

Definice problému Střídavé odprašování vrstev materiálu a snímání povrchu vzorku právě v tomto místě je jednou z metod destruktivní 3D analýzy vzorku ve skenovacím elektronovém mikroskopu, doplněném o generátor iontového svazku umožňující rychlejší odstraňování materiálu. Princip metod pro měření tloušťky odprášených vrstev spočívá v detekci image features a počítání jejich vzájemných vzdáleností v obrázcích nasnímaných během procesu odprašování materiálu. Je žádoucí, aby byly metody nejen přesné, ale i dostatečně praktické, a tedy snadno zasaditelné do samotného procesu 3D analýzy bez toho, aniž by jej výrazněji zpomalovaly.

Kromě toho je třeba navrhnout a implementovat způsob pro získání ground truth, aby bylo možné naměřené výsledky vyhodnotit. Vzhledem k tomu, že účelem metody pro získání ground truth je pouhé ověření přesnosti výsledků naměřených zbylými metodami, není nutné klást u ní přehnaný důraz na praktičnost, avšak, je zásadní, aby dostatečně přesně reflektovala reálné hodnoty.

Existující řešení V roce 2010 byla publikována doposud jediná existující Chevrons metoda spočívající ve vypálení dvou čar ve tvaru "V" do povrchu vzorku iontovýn svazkem a výpočtu tloušťky odprášených vrstev měřením vzdáleností detekovaných pozic těchto čar v po sobě jdoucích obrázcích. Díky zvolenému rozložení obou čar se totiž vzdálenost jejich pozic s přibývajícím množstvím odprášeného materiálu postupně mění. Nutnost vytvoření tohoto vzoru ve tvaru "V" ještě před samotným začátkem odprašování materiálu a snímání vzorku však celý proces měření zbytečně zdržuje a činí tak Chevrons metodu nepraktickou z hlediska uživatelského použití.

Navržené řešení Tato práce představuje dvě alternativní metody (Top-Down FIB a Y-Shift SEM) využívající k měření tloušťky odprášených vrstev detekci image features, které se na povrchu vzorku již vyskytují, takže je není třeba vytvářet. Jednou z těchto features je vodorovná hranu vzorku, v jejímž místě dochází k odstraňování vrstev materiálu, což má za následek její postupně měnící se pozici. U druhé image feature je pak nutné, aby svou pozici v čase neměnila. Výsledná tloušťka odprášených vrstev je pak určena jako rozdíl vzdáleností detekovaných pozic takových dvou features v po sobě jdoucích obrázcích. Obě navržené metody stojí na tomtéž principu a liší se pouze v tom, jakou zobrazovací technologií (elektrony či ionty) a pod jakým pozorovacím úhlem pro ně byly pořízeny vstupní obrázky.

Mimo to přicházím s návrhem metody pro získání ground truth k samotnému měření. Základem metody je vypálení pravidelného vzoru stovek drobných jamek (teček) do povrchu vzorku, blízko jeho vodorovné hrany, ještě před samotným začátkem procesu odprašování vrstev materiálu. Po každém odprášení vrstvy materiálu pak zmizí z povrchu vzorku, a tedy i z obrazu, určitý počet těchto teček, což znamená, že skutečnou tloušťku vrstev

odprášeného materiálu lze určit jako rozdíl zdetekovaného počtu teček ve dvou po sobě jdoucích obrázcích, neboť rozměry samotného tečkovaného vzoru jsou předem definované.

Implementace navržených metod Pro detekci vodorovné hrany vzorku, využívané oběma navrženými metodami měření, používám vlastní algoritmus spočívající v průměrování hodnot intenzit pixelů v jednotlivých řádcích obrázku a následné konvoluci s druhou derivací Gaussovy funkce. Na rozdíl od běžně používaných hranových detektorů je dostatečně robustní k obrázkům vodorovné hrany vzorku, jejíž podoba je v obraze často rozmazaná a nekonzistentní. Druhou image feature, jíž je typicky vzor křížku používaný jako image matching reference pro odprašování vrstev materiálu, detekuji interní implementací firemního algoritmu založeného na discriminative correlation filters.

Samotný algoritmus detekce teček, rozložených ve vzoru v deseti téměř vodorovných řadách po třiceti šesti, nejprve namapuje nepravidelnou mřížku na jednotlivé tečky v obraze a následně počítá vzájemnou podobnost obrázků jednotlivých polí mřížky, odpovídající pozicím teček ve vzoru, aby zjistil, s jakou pravděpodobností se v polích tečky skutečně nachází. Prahováním hodnot podobnostního skóre pak lze tečky v obraze spočítat.

Experimenty a dosažené výsledky Pro účely vyhodnocení jednotlivých metod a algoritmů jsem vytvořil tři datové sady po dvanácti, resp. třinácti obrázcích vzorku v mikroskopu. Porovnání naměřených výsledků ukázalo, že jak Chevrons metoda, tak Top-Down FIB metoda měří tloušťku vrstev konzistentně, neboť jimi naměřené hodnoty mají stabilní odchylku od ground truth ve všech třech provedených měřeních. Navíc, odchylka Top-Down FIB metody je znatelně nižší, díky čemuž ji lze označit za nejpřenější ze všech tří meřicích metod. Y-Shift SEM metoda se naopak jeví značně nestabilně. Kromě toho výsledky naznačují, že algoritmus detekce teček je skutečně použitelnou metodou k získání ground truth pro měření, neboť na dostupných datech dosáhl stabilnějších výsledků, než alternativní hodnoty ground truth vygenerované manuální anotací jednotlivých obrázků.

Závěr Cíl práce lze označit za splněný z následujících dvou důvodů: Zaprvé, byla navržena a implementována měřicí metoda, jež je nejen praktičtější, než metody existující, ale na dostupných datech dosahuje také o něco vyšší přesnosti. A zadruhé: Byl vyvinut algoritmus pro získání ground truth k hodnotám tloušťky odprášených vrstev naměřeným jednotlivými metodami a prokázal se býti použitelnou metodou produkující stabilní výsledky. Pro vyvození jasnějších závěrů o přesnosti jednotlivých metod však bude třeba metody vyhodnotit na více datech, než na kolika tomu bylo v nynějších experimentech.

Measuring the thickness of material layers removed from a sample in an electron microscope

Declaration

I hereby declare that this Master's thesis was prepared as an original work by the author Jiří Kutálek under the supervision of doc. Ing. Martin Čadík, Ph.D. I have listed all the literary sources, publications and other sources, which were used during the preparation of this thesis.

. . . .
Jiří Kutálek
May 16, 2023

Acknowledgements

I would like to sincerely thank my consultant Ing. Bronislav Přibyl, Ph.D. and my supervisor doc. Ing. Martin Čadík, Ph.D. for their help, guidance and motivation during the work. I would also like to thank my colleagues from the Thermo Fisher Scientific company, Ing. et Ing. Dávid Pacura for supervision, and both Ing. Jiří Víteček and Mgr. František Zelenka, Ph.D. for their tips related to the process of data acquisition.

Contents

1 Introduction **2**

2 Scanning Electron Microscopy **3**
2.1 Motivation for the Electron Microscopy Technique . . . 3
2.2 Scanning Electron Microscopy Principles . . . 4

3 Typical Workflow of the Dual-beam Microscopes **8**
3.1 Focused Ion Beam . . . 8
3.2 Slice And View Workflow . . . 9

4 Existing Methods for Material Layers Thickness Measurement **12**
4.1 Pattern of Two Longitudinal Marks . . . 12
4.2 Calculating the Slice Thickness . . . 13

5 Discussion of the Existing Solution **14**
5.1 Method Evaluation . . . 14
5.2 Room for Improvement . . . 15

6 Proposed Methods for the Material Layers Thickness Measurement **16**
6.1 Top-Down FIB Method . . . 16
6.2 Y-Shift SEM Method . . . 18
6.3 Implementation of the Measurement Methods . . . 19

7 Ground Truth Establishment **26**
7.1 Preparations for the Ground Truth Establishment . . . 26
7.2 Using the Referential Pattern for Ground Truth Generation . . . 28
7.3 Manual Ground Truth Alternative . . . 34

8 Experimental Results **35**
8.1 Acquired Data for the Experiments . . . 35
8.2 Evaluation of the Methods . . . 39

9 Conclusion **44**

Bibliography **45**

A Contents of the included storage media **46**

Chapter 1

Introduction

Scanning electron microscopes are used for observing a sample by scanning its surface by a beam of electrons. Combined with a focused beam of ions, capable of a fast removal of material layers from the surface, it is used to obtain a 3D sample analysis by iteratively removing layers of material and imaging the sample surface, from which the material was removed. However, the thickness of removed material layers is practically not identical for each of the individual layers, so in order to obtain a proper 3D reconstruction of a sample volume, the thickness of each layer must be known.

There are techniques for measuring the thickness of removed material layers. Unfortunately, the existing ones are impractical and their actual accuracy is unknown. This study proposes new measurement methods, which are more effective from the practical point of view, and introduces an approach for obtaining the ground truth for the measurement, serving as a technique for evaluating the accuracy of the proposed methods.

The objective of this thesis is to get familiar with electron microscopy and its image characteristics, study existing methods for measuring the thickness of removed material layers from a sample in a scanning electron microscope, propose new methods improving the existing ones, experiment with them and evaluate their accuracy, and at the end, discuss the results and applicability of the proposed methods. It should be pointed out that the main goal of this work is coming up with new solutions, which are more effective than the existing methods, and finding a way of practically using them.

As for the structure of this thesis, Chapter 2 introduces the concept of a scanning electron microscope, outlying its structure and describing the process of image formation using an electron beam. After the explanation of how does a SEM equipped with a focused ion beam look like and presenting the typical workflow for an iterative removal of material layers and imaging a sample surface in Chapter 3, the existing methods for measuring the thickness of such material layers are described in Chapter 4. The following Chapter 5 interconnects the study part of this thesis with the chapters related to the actual work done, discussing the existing solutions, suggesting possible improvements and defining the goals of this thesis. After that, Chapter 6 introduces two methods proposed as an alternative to the state-of-the-art solution, explains their principles and presents an algorithm for implementing them. In Chapter 7 the approach for obtaining the ground truth for the measurement is described, including an algorithm implementing it. Finally, the experimental results of the methods performance on the available data are presented and discussed in Chapter 8.

Chapter 2

Scanning Electron Microscopy

This Chapter introduces the concept of a scanning electron microscope capable of producing images of a sample[1] being observed by scanning its surface by a beam of electrons.

At the very beginning the motivation behind the usage of electrons in microscopy techniques is declared. Subsequently, two main types of electron microscopes are presented and compared. The rest of the Chapter focuses entirely on scanning electron microscopes, outlying their structure consisting of an electron column and a sample chamber, and explaining the process of image formation using an electron beam scanning over the sample surface.

2.1 Motivation for the Electron Microscopy Technique

Before digging deeper into the scanning electron microscopy principles, it should be stated which tasks are examined by the electron microscopy methods and what are their advantages over the other existing techniques. There are two main microscopic fields, the optical microscopy and the electron one. This Section compares their principles and explains why are the electron microscopes capable of solving the problems questioned in this thesis.

2.1.1 Optical Microscopy

Using visible light as an illumination source, an **optical microscope** is simple and easy to maintain. Additionally, the optical models are much cheaper compared to the electron ones, as they do not require an external electrical source. However, their resolution is theoretically limited to approximately one-half the wavelength of visible light (200 nm) [1].

2.1.2 Electron Microscopy

In contrast to an optical microscope, an **electron microscope** uses an electron beam as the source of illumination. As the wavelength of electrons can be thousands times shorter than that of visible light photons, the electron microscope is capable of reaching much higher resolution (some types can do better than 1 nm, as depicted in Figure 2.1) and, therefore, is used to observe far smaller structures than can be visualized using an optical microscope.

[1] It should be noted that the expression “sample” relates to the specimen being observed in a microscope in this thesis and has nothing in common with a value of a signal at a particular point in time or space.

[2] https://www.pngwing.com/

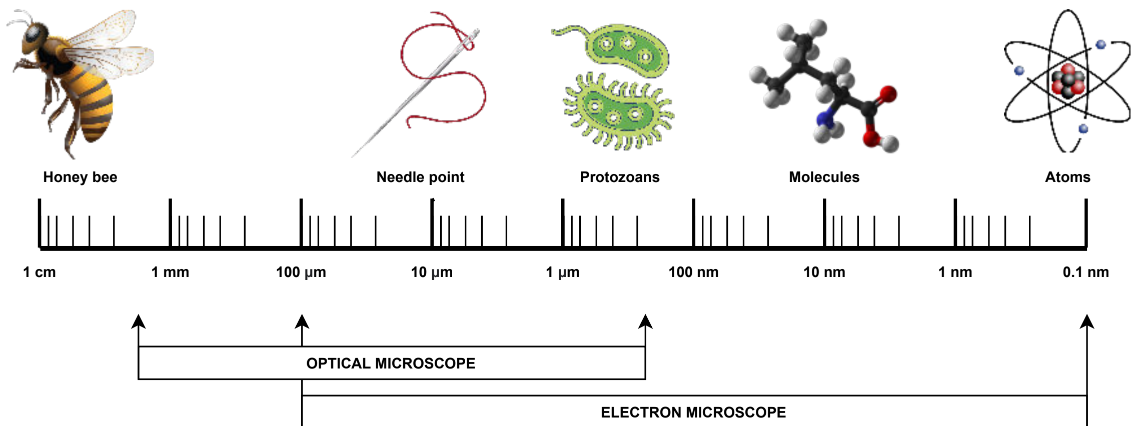

Figure 2.1: An illustration showing an approximate difference in magnification capabilities of the optical and the electron microscopes. All of the individual images were taken from the *PNGWing* website[2].

Nevertheless, due to the fact that electrons are fired to interact with the sample being observed, there is a risk of damaging the sample by the electron beam, which is a notable disadvantage of this approach, compared to the photon-based principle.

2.2 Scanning Electron Microscopy Principles

After introducing the two major types of electron microscopes, the transmission and the scanning ones, the physics behind the scanning process and the image formation is explained in this Section, including a closer look onto the design of an electron column, propagating a beam of electrons towards the observed sample. Besides, basic information about the sample positioning in chamber is presented too.

2.2.1 Types of Electron Microscopes

The type of an electron microscope used to look at thin sections of material is known as a **transmission electron microscope (TEM)**. This is, in principle, similar to an optical microscope, except that it transmits a beam of electrons rather than a beam of light through the sample [2]. The resulting image is obtained by collecting the electrons, which passed through the sample inner structure.

Another type of an electron microscope, a **scanning electron microscope (SEM)**, scatters electrons off the surface of a sample and so is used to provide information about the surface of a sample, unlike the TEM, which provides data about the sample inner structure. Both types are depicted and compared in an illustration in Figure 2.2.

Note that this thesis concentrates merely on SEMs, whose functionality is presented more in detail in the following part of this Section.

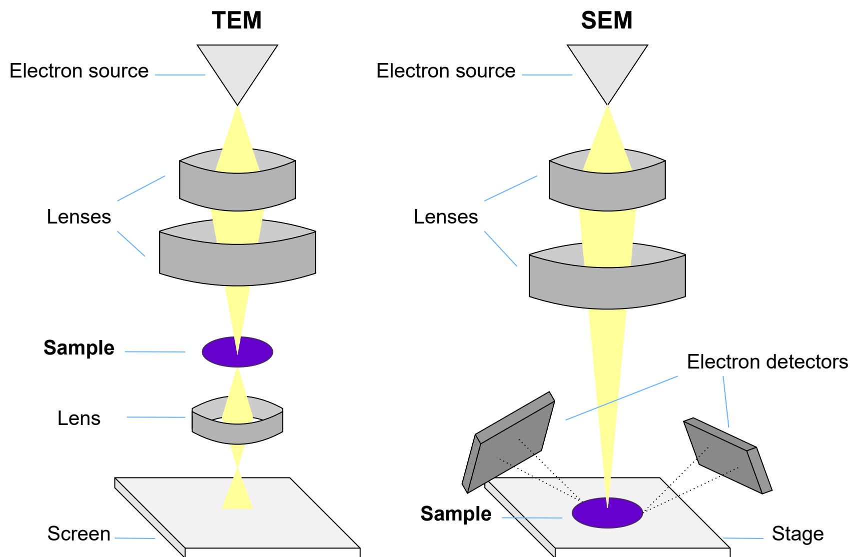

Figure 2.2: An illustration showing schematic diagrams of both transmission and scanning electron microscopes. In TEM **(left)** the electrons **(yellow)**, produced by an electron source, are passed through a sample **(purple)**, and the resulting image, formed by the interaction of the electrons with the sample, is magnified onto a viewing screen. Conversely, in SEM **(right)** the electron beam does not penetrate through the whole sample volume. Instead, it raster-scans across the sample surface and the detectors collect the electrons emitted from the surface.

2.2.2 Image Formation

The SEM instrument can be considered to comprise of an **electron column** and a **sample chamber**. The schematic in Figure 2.3 shows components located within the column and the chamber, which are responsible for the process of scanning an electron beam of high energy on the sample surface to obtain images [3].

Scanning Process The electron gun located at the topmost section of the column generates an electron beam, which is focused into a fine probe by electromagnetic lenses located within the column. The fine electron probe is then rastered over the sample surface in a rectangular area by scanning coils, which are also present within the column. A SEM produces single channel grayscale images (colors can be added later, during the post-processing).

The sample itself is present in a chamber that is located at the end of the column. Both the column and the chamber are kept under vacuum, to allow the electron beam generation and prevent its interaction with air molecules.

Sample Positioning The sample to be examined is loaded onto a holder that is placed on a stage. Some of the modern stages are capable of moving in five different directions: apart from shifting in the up/down, left/right and forward/backward directions corresponding to the x, y and z axes, a stage can also perform a rotation around its vertical axis and a tilt.

[3] `https://www.thermofisher.com/cz/en/home/electron-microscopy/products/dualbeam-fib-sem-microscopes/helios-5-pfib-dualbeam.html`

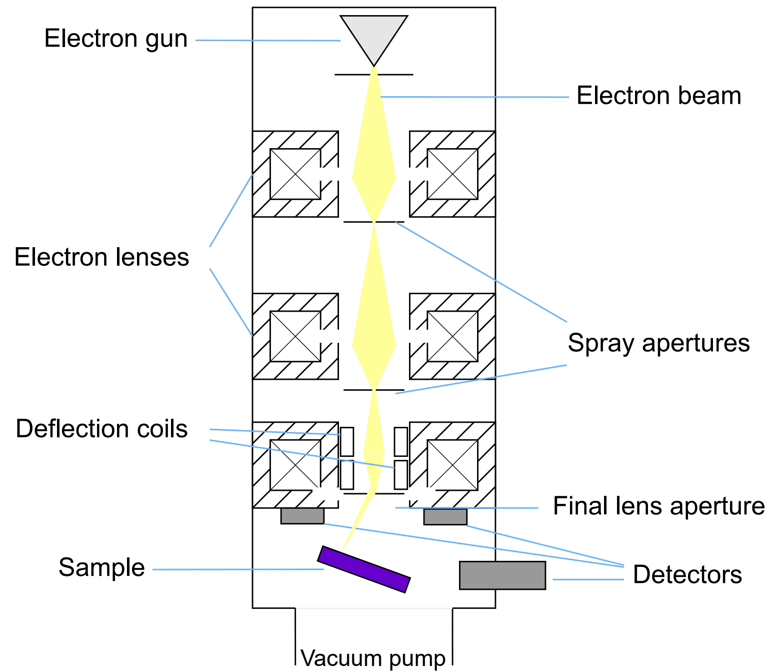

Figure 2.3: A schematic drawing of an electron column and a sample chamber, inspired by the original illustration presented in the book from Goldstein et al. [4]. The electron column consists of an electron gun generating a beam of accelerated electrons **(yellow)**, electromagnetic lenses located within the column focusing the beam into a small diameter (few nm) probe and scanning coils deflecting the probe, so that it scans over the surface of a sample. The end of the column ends up in the chamber, both kept under vacuum, in which the sample **(purple)** is located. An output image is produced by detecting signals generated by the electron beam penetrating into the sample surface [3].

To fit on the stage and the holder, a SEM sample area size hardly ever reaches 1cm^2. In spite of that, it may be of a wide range of material types, such as solid metals or soft biological samples. The illustration in Figure 2.4 provides a look into the chamber, showing the sample positioning on the stage with respect to the end of the electron column.

Instabilities As mentioned, the SEM images are acquired using an electron beam scanning across a sample surface. Related to the fact that the electron beam position is controlled by electromagnetic lenses and the magnification can be very large (up to the order of millions), the images may contain positional errors caused by various factors, such as variations in electromagnetic field, environment temperature, vibrations or sample charging. Changes of such positional errors over time is referred to as a drift distortion or an image drift [5].

Apart from that, to be used properly, it is important to calibrate the magnification of the SEM. This can be accomplished with a calibration sample, a sample that contains features with defined distances, whose dimensions are traceable to the fundamental primary length standard through a national measurement institution [6]. Without doing this, the magnified output images might have distorted scale.

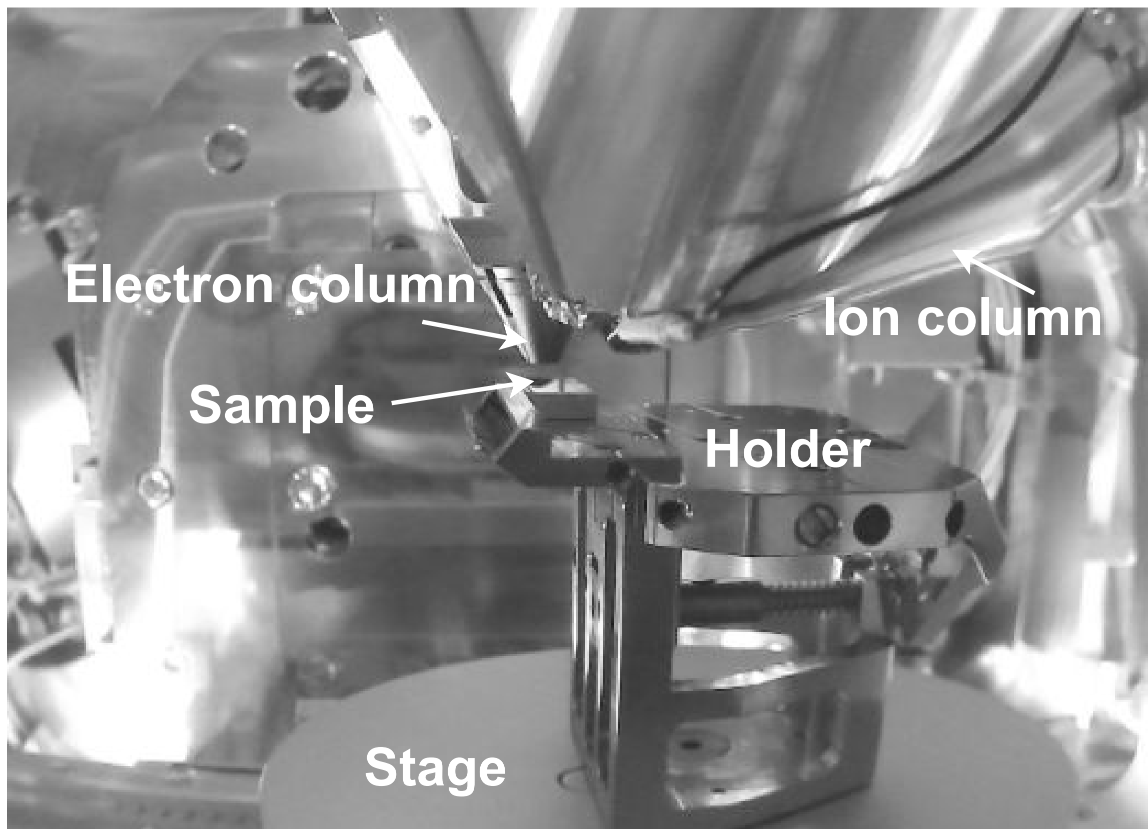

Figure 2.4: A picture showing the inside of a real microscope chamber[3]. The **sample** mounted on a holder sits on the **stage**. In this case, the stage is tilted to 0° (not tilted), and so the electron beam, coming from the **electron column**, aims perpendicularly to the sample surface. Additionally, an **ion column** can be observed in the image as well, serving as an ion beam source, which is introduced in the following Chapter 3.

Chapter 3

Typical Workflow of the Dual-beam Microscopes

Although the previous Chapter 2 states that this thesis focuses exclusively on SEMs, the area of interest is even more specific, as all the microscopes related to the investigated problem of measuring the thickness of material layers removed from a sample are so-called **dual-beam scanning electron microscopes (FIB-SEMs)**, which are special types of scanning electron microscopes.

A FIB-SEM is a SEM equipped with a focused ion beam (FIB), giving the possibility of using a beam of ions instead of a beam of electrons for a faster material removal. This Chapter introduces the concept of a FIB and describes its integration with a SEM, creating a FIB-SEM (a dual-beam microscope).

3.1 Focused Ion Beam

Microscopes utilizing a focused ion beam (FIB) work analogously to the ordinary SEMs, rastering a beam of particles over the sample surface with the resulting signal at each raster position plotted to form an image [4]. The major difference is that instead of electrons, a FIB uses a beam of positively charged ions – atoms or molecules with an electrical charge.

Advantage of Using Ions Ions are heavier than electrons and carry a greater momentum, meaning that the use of positively charged heavy ions makes it easier to remove material from a sample. Therefore, a FIB is useful for milling, ablation, or even deposition of materials. The material removal and deposition can be controlled to a nanometer scale and different gases can be injected into the system near the surface of a sample to deposit required materials [3]. At lower beam currents a FIB can be used for a sample imaging too.

Ion Column Characteristics The structure of a typical focused ion beam column resembles a simple SEM column, as the one depicted in Figure 2.3, with the exception that the magnetic lenses that are used to focus electrons are not capable of focusing the heavier ions. For ions, the lenses are electrostatic and require high voltages to focus energetic ions due to their relatively large mass to charge ratio [6].

3.1.1 Dual-beam Systems

The FIB-SEM microscopes are two-column systems with a FIB column and a SEM column (an electron column) mounted on one chamber with the aim of both columns focusing precisely on the same region of a sample [6]. This allows one to use a SEM column to monitor the progress of the FIB milling (the process of material removal using a FIB) that is being performed and to image the sample immediately after milling. This concept is illustrated in Figure 3.1.

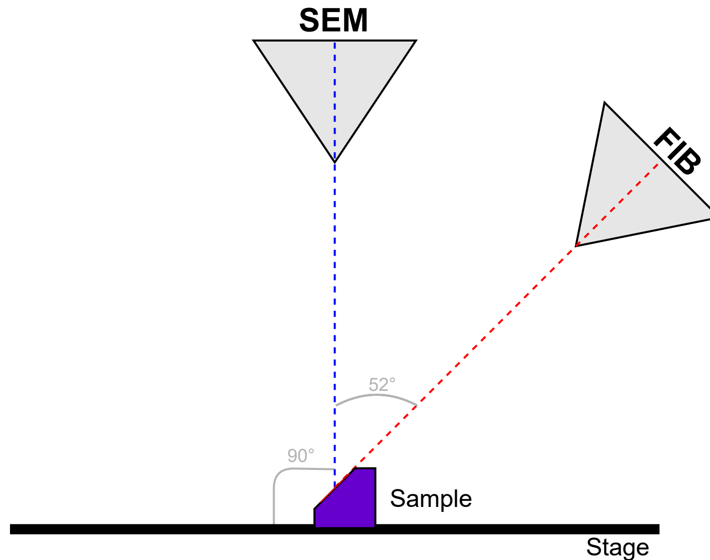

Figure 3.1: A schematic showing a combined usage of the SEM and FIB columns, in which the FIB is used to mill away material to expose a cross-sectional view of the sample and the SEM is used for the image acquisition, both generating a beam of particles from a different angle with respect to the sample surface. In this typical configuration, the angle between both of the columns is 52°.

The FIB-SEM workflow, comprising of repetitively removing layers of material and then imaging the sample surface from which the material was removed is one of the methods for destructive 3D sample analysis and is discussed more detailed in the following Section 3.2.

3.2 Slice And View Workflow

The FIB-SEM arrangement allows the use of sequential FIB milling and SEM imaging (acquiring images of a sample using an electron column)[1], leading to the capability of producing 3D datasets. This technique is often referenced as the FIB-SEM workflow or the Slice And View approach[2].

The Slice And View workflow comprises of two iteratively repeating stages, known as **slicing** and **imaging**. This process is destructive, because material is being sequentially milled away from a sample before and after each imaging step.

[1] Note that from this point the "SEM" expression typically refers to a beam electrons, analogously to the "FIB", not the entire microscope.

[2] "Slicing" refers to the process of material removal from a sample surface, as well as "milling", but more specifically, as is it describes "milling" in a way of iteratively removing material layers.

3.2.1 Slicing And Imaging

Layers of material are usually milled away using a FIB, as due to the fact that the ions are much heavier that the electrons the process is much faster. After each such slicing step, the **cut-face** can be immediately imaged with the SEM that is at some inclined angle with respect to the ion beam [6]. This approach is illustrated in Figure 3.2

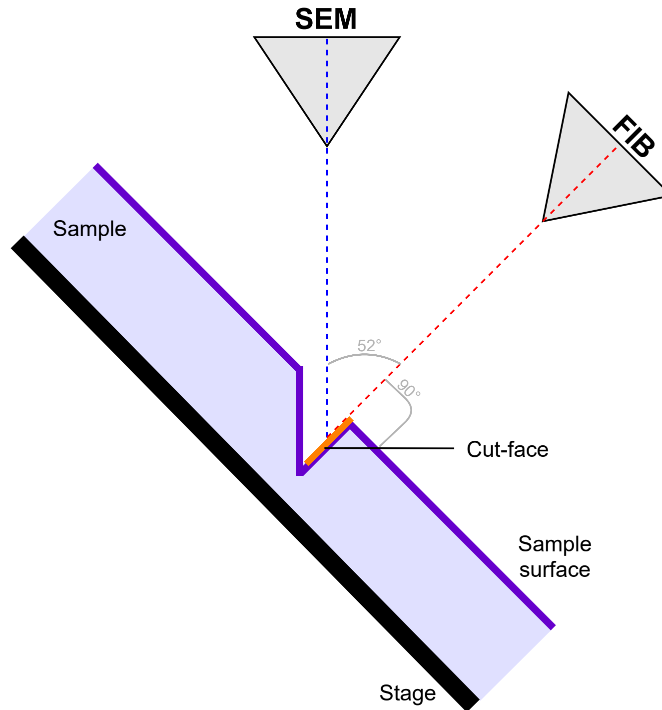

Figure 3.2: A schematic illustrating the Slice And View approach consisting of a FIB performing the slicing of material layers and a SEM imaging the cut-face. In this case, the stage is tilted to a position, which is perpendicular to the ion beam column so that it can dig below the surface, whilst the electron column images the cut-face exposed by the FIB.

It is worth pointing out that the imaging can be performed by a FIB, alternatively. The FIB imaging offers a lesser resolution compared to the SEM imaging, as the electron beam is more focused than the ion one, but provides a greater image contrast as that provided by the SEM.

The complete Slice And View workflow is enumerated in the following listing:

1. Prepare the sample area for slicing, including an initial cut-face exposure and placing a referential feature mark for image matching.
2. **Slicing:** Mill away a layer of material from the cut-face using a FIB.
3. **Imaging:** Acquire an image of the cut-face or the sample surface (using either a FIB or a SEM).
4. Repeat steps (2) and (3) for a defined number of times – slice a number of material layers and generate the same number of images corresponding to them.
5. After acquiring all the images, create a 3D sample volume reconstruction from them.

Figure 3.3 shows a real example of cross-sectional slicing done by the FIB and imaged by the SEM, including a real visualization of a sample surface, a cut-face and a **cut-face edge** between them. The positions of both of the columns in the illustration correspond to the column positions in the schematic depicted in Figure 3.2.

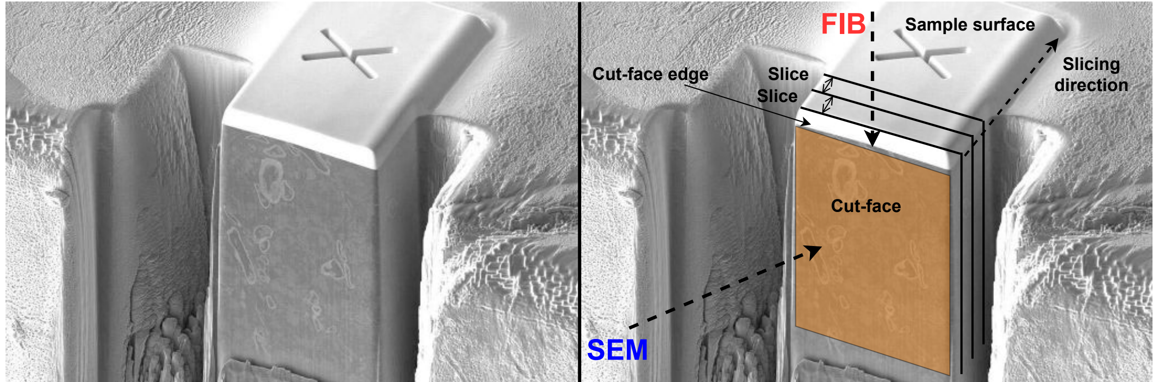

Figure 3.3: Example of a cross-sectional cut made into a sample using a FIB aiming perpendicularly to the sample surface. The image, originally published at the Thermo Fisher Scientific web page[3], was acquired using a SEM from a slanted angle. The original image **(left)** is augmented with descriptive drawings **(right)**. Both the SEM and the FIB directions are marked by the **blue** and **red** dashed arrows. In the direction indicated by the **black** dashed arrow individual slices of material are consecutively being milled away from the cut-face **(orange)** by the ion beam. The cut-face edge is located on the top of the cut-face adjacent to the sample surface.

3.2.2 Slice Thickness Parameter

The Slice And View workflow produces a set of slice images[4] together forming a 3D reconstruction of a sample volume. In this process, an important user-definable parameter are the distances between the individual slices.

Practically, these are not equidistant. However, to obtain a correct 3D reconstruction of a sample volume, the slices either should be equidistant, or their distances must be known.

In other words, the distance between each two individual slices, referred to as the **slice thickness**, is an important parameter that has to be measured, because without knowing it, the resulting 3D reconstruction cannot be obtained properly.

[3] `https://www.thermofisher.com/cz/en/home/electron-microscopy/products/dualbeam-fib-sem-microscopes/helios-hydra-dualbeam.html`

[4] The “slice image” expression refers to an image of either the sample surface or the cut-face acquired immediately after a slice was milled away using a FIB, in this thesis.

Chapter 4

Existing Methods for Material Layers Thickness Measurement

There is a paper [7] that investigates whether slice thickness values change with the depth of the cut-face, by stacking layers of high and low contrast material with known geometry. However, this issue is not exactly the same as the one being addressed in this thesis.

In May 2010, Edward Principe proposed a solution [8] lying in creating a pattern of longitudinal marks on the top of a sample surface. In consecutive images, the positions of these marks are detected and used to quantify the thickness of removed material layers.

Due to the fact that this is the only published solution so far, this Chapter focuses entirely on description of this state-of-the-art method.

4.1 Pattern of Two Longitudinal Marks

The "chevron pattern" consists of two longitudinal marks carved into the sample surface, having an angle between each other. In Figure 4.1 there are two schematics showing the pattern shape and its position when placed on a sample surface.

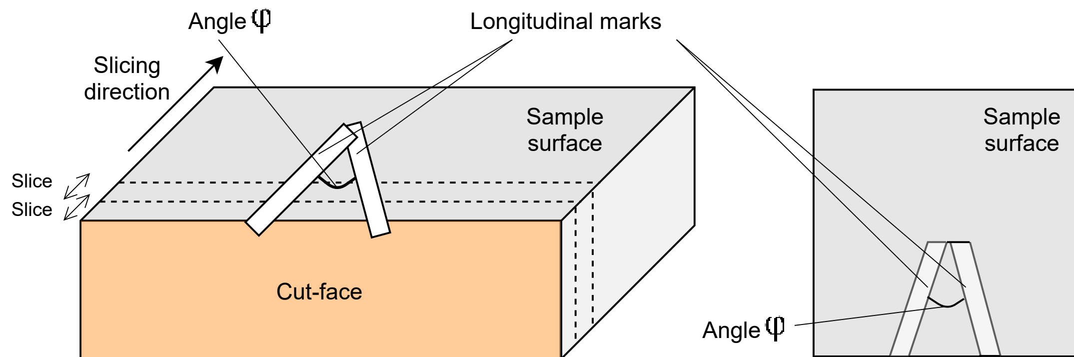

Figure 4.1: According to the invention [8], two longitudinal marks are placed on the surface of a sample before the start of the slicing process. Because the marks include the angle ϕ between, the position of the marks in each slice image changes each time a slice is removed. By identifying the positions of the marks at the cut-face **(orange)** and comparing them in consecutive images the thickness of material layers, milled away by a FIB in the slicing direction **(black arrow)**, can be measured.

4.2 Calculating the Slice Thickness

The calculation of the slice thickness values based on the chevron pattern placed on a sample surface can be performed by comparing similar triangles, as shown in Figure 4.2, using a formula in the following Equation (4.1):

$$\Delta t = \frac{A_{n-1} - A_n}{\tan \theta} \tag{4.1}$$

Using the formula presented above, the Δt, defining the slice thickness, corresponds to the ratio of the difference of chevrons positions in two consecutive slices A_{n-1} and A_n, and the tangent of the θ angle that form the longitudinal marks between them. To see an illustration related to this calculation, see the schematic presented in Figure 4.2.

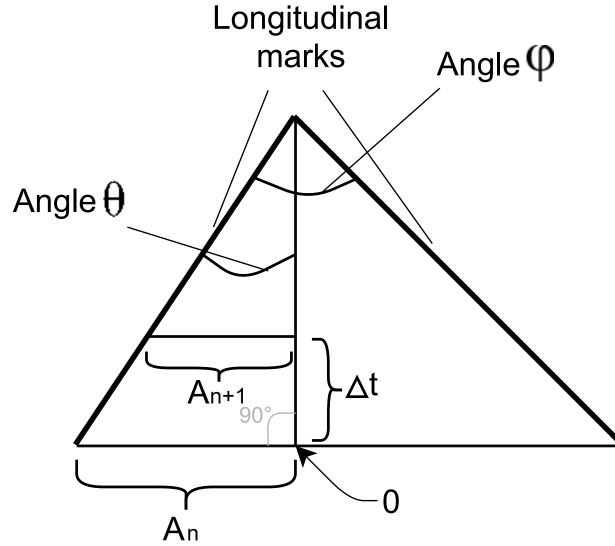

Figure 4.2: According to the paper [8], a slice thickness value can be determined knowing the distances of positions A_{n-1} and A_n of the mark in two consecutive images n and $n+1$ from an arbitrarily defined zero point, and the angle θ, which the left longitudinal mark includes with an axis perpendicular to the slice plane. Note that when the angle θ equals to a half of the angle ϕ, which usually does when used in practice, the zero point lies in the middle of the bottom side of the triangle.

Usage In the Slice And View Workflow After completing the entire slicing process, consisting of iterative slice removing and subsequent image acquiring, presented step-by-step in Section 3.2, all of the slice images in the acquired dataset are analyzed. In each of them the positions of the chevrons are detected and the slice thickness values are calculated as the differences between the positions in each two consecutive slice images.

Chapter 5

Discussion of the Existing Solution

Chapter 4 presented an elegant state-of-the-art solution for the slice thickness measurement problem. According to the proposed method [8], the slice thickness of each removed material layer is quantified using a geometrical relationship between two marks of a chevron pattern placed on the sample surface.

This approach has several advantages in terms of a practical usage, but unfortunately, a few notable drawbacks as well. This Chapter discusses both of these and makes suggestions of further improvements. At the end, the goals of this project are set.

5.1 Method Evaluation

Advantages Because the method does not require a different stage position than the one used for slicing, the measurement process suffers no errors caused by a mechanical stage movement (translation, rotation or tilt) – there is no extra stage movement needed, because the slice thickness is measured from images acquired at the same stage position as the slicing is done. Moreover, the superfluous stage move would have slowed the Slice and View process, which would be an unwanted effect as the speed of the entire process is a critical parameter from a user point of view.

In addition, all the information needed for the measurement process, meaning an image of the cut-face containing the cross-section of the longitudinal marks, is already in a slice image acquired during the data acquisition process. The slice thickness measurement method does not require any additional information apart from these already present in the slice images, which is convenient too.

Sample Preparation Requirement However, there is still the prerequisite of creating the chevron pattern before the actual Slice and View process, in order to be able to obtain the slice thickness values at the end of it. This sample preparation step slows the entire process and adds an extra overhead, as until a chevrons pattern is not placed on a sample surface, the slicing and imaging cannot start.

5.2 Room for Improvement

From a user point of view, it would be much better if there are no such redundant preparation steps needed before the Slice and View process. Thus, I believe that there is definitely a room for improvement, for coming up with a method not requiring the sample preparation step. Designing such a method is the primary goal of this thesis.

Absence of Ground Truth Bringing a faster and more efficient slice thickness measurement method is set as the main objective of this project, but despite proposing it, it would be appropriate to evaluate the accuracy of such a method and to compare it with the state-of-the-art Chevrons method.

Nevertheless, the accuracy of the Chevrons method is unknown, as its associated approach calculates the slice thickness from a series of images, but there is no assurance that the feature positions detected in image exactly correspond to the actual, real-world values. According to that, an evaluation of the individual methods accuracy cannot be determined and their comparison is clearly not possible, because there is no ground truth value to compare with.

Therefore, finding a way to obtain the ground truth for the measurement, serving as a technique for evaluating the proposed slice thickness measurement method and comparing it with the state-of-the-art one is set as the secondary goal of this thesis.

Chapter 6

Proposed Methods for the Material Layers Thickness Measurement

The first part of this Chapter presents two new methods for measuring the thickness of removed material layers from a sample, describes their principles and points out their advantages compared to the state-of-the-art Chevrons method. The last Section of the Chapter focuses on describing the implementation of all the measurement methods.

The proposed methods have two advantages: First, they do not introduce any additional stage movements to the Slice And View process, and second, they do not require any pattern placement on the sample surface, as the Chevrons method does, or any other kind of time-consuming sample preparation. Note that the idea behind both methods originates from my colleagues from the Thermo Fisher Scientific company.

6.1 Top-Down FIB Method

The Top-Down FIB method uses a FIB for both slicing and image acquisition. Having the sample stage tilted to a position, in which a sample surface is perpendicular to the ion beam column, material layers are milled away from the cut-face as usual and images of the sample surface are acquired from the top-down view of the FIB. This principle is illustrated in Figure 6.1.

Measuring the Slice Thickness The actual slice thickness is calculated as a difference of distances from the cut-face edge to another significant feature in the image, in two consecutive slice images. Figure 6.2 shows an example of such two images from a dataset acquired for the Top-Down FIB method evaluation, illustrating the idea behind this approach.

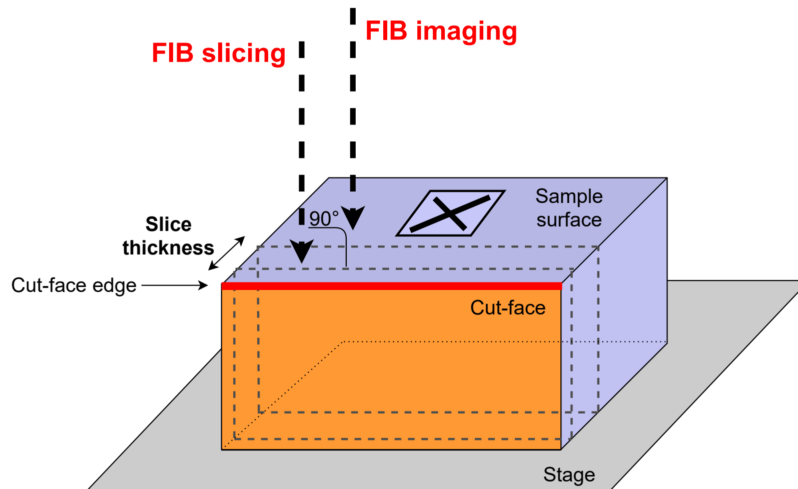

Figure 6.1: A schematic showing the principle of the Top-Down FIB method used for the slice thickness measurement. A FIB aims perpendicularly to the surface of a sample **(purple)**, both slicing material layers from the cut-face **(orange)** and acquiring images from its top-down view. The cross-mark serves as a reference feature for the actual measurement.

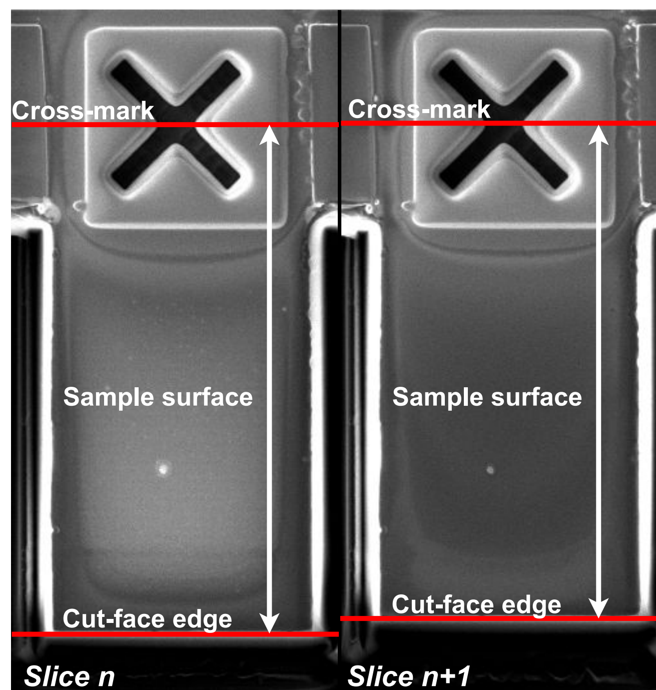

Figure 6.2: Example of two consecutive slice images acquired using the Top-Down FIB method. In order to calculate the slice thickness for the n–th slice, a cut-face edge position **(bottom red lines)** is detected in both images, as well as the position of the cross-mark **(top red lines)** etched into the sample surface and their distance in image is measured **(white double arrows)**. The resulting slice thickness value is determined as a difference of these distances.

6.2 Y-Shift SEM Method

Apart from the Top-Down FIB, there is a proposal of another, alternative method, referred to as the Y-Shift SEM[1]. Unlike the Top-Down FIB method imaging the sample surface using the ion beam column, it uses SEM for acquiring slice images of the cut-face. The idea behind it is depicted in Figure 6.3.

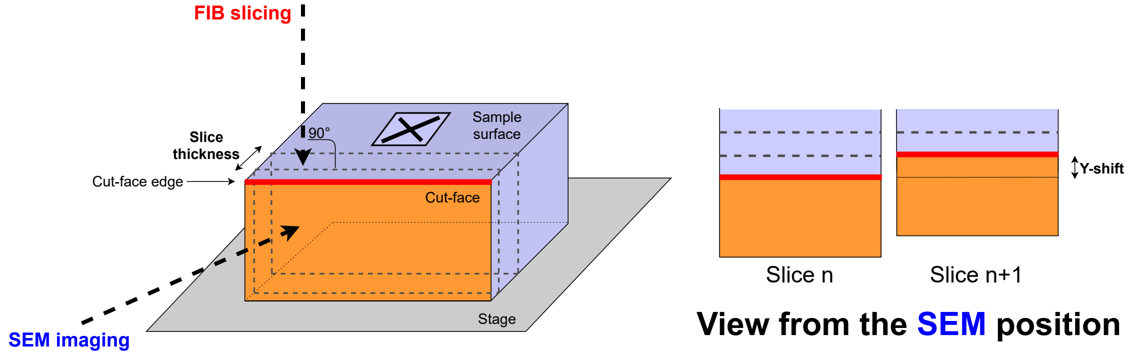

Figure 6.3: A schematic showing the Y-Shift SEM method principle. Unlike the Top-Down FIB, it uses the FIB only for slicing and the slice images are acquired by the SEM, imaging the cut-face **(orange)**. Similarly to the Top-Down FIB, the slice thickness values are determined as the differences of measured distances from a cut-face edge **(red)** to another, fixed image feature in consecutive slice images.

Measuring the Slice Thickness Knowing the geometry of the cut-face and the sample surface, and the image acquisition angle, the slice thickness values are calculated from the measured y-shift (as illustrated in Figure 6.3). Similarly to the Top-Down FIB method, the Y-Shift SEM needs another fixed reference feature for measuring the distance to the cut-face edge, and the subsequent slice thickness calculation. Figure 6.4 shows an example of a slice image with a highlighted cut-face edge illustrating the method's principle.

6.2.1 Correction of the Measured Values

Due to the fact that the SEM acquires images from an angle for the Y-Shift SEM method, the measured image feature distances are shorter than the actual ones, resulting in distorted slice thickness values. Therefore, the slice thickness values measured by the Y-Shift SEM method must be corrected multiplying them by a constant compensating the non-perpendicular view angle.

A formula for calculating such correction is presented in Equation (6.1). An illustration in Figure 6.5 shows the intuition behind the calculation.

$$s = \frac{y}{\cos 52°} = \frac{y}{\sin 38°} \tag{6.1}$$

where s stands for the corrected slice thickness value and y refers to a value measured by the Y-Shift SEM method in an image acquired by SEM from an angle. The deduction

[1]The phenomenon of an apparent movement the cut-face position in the y-direction in image after material removal, is referred to as the "Y-shift".

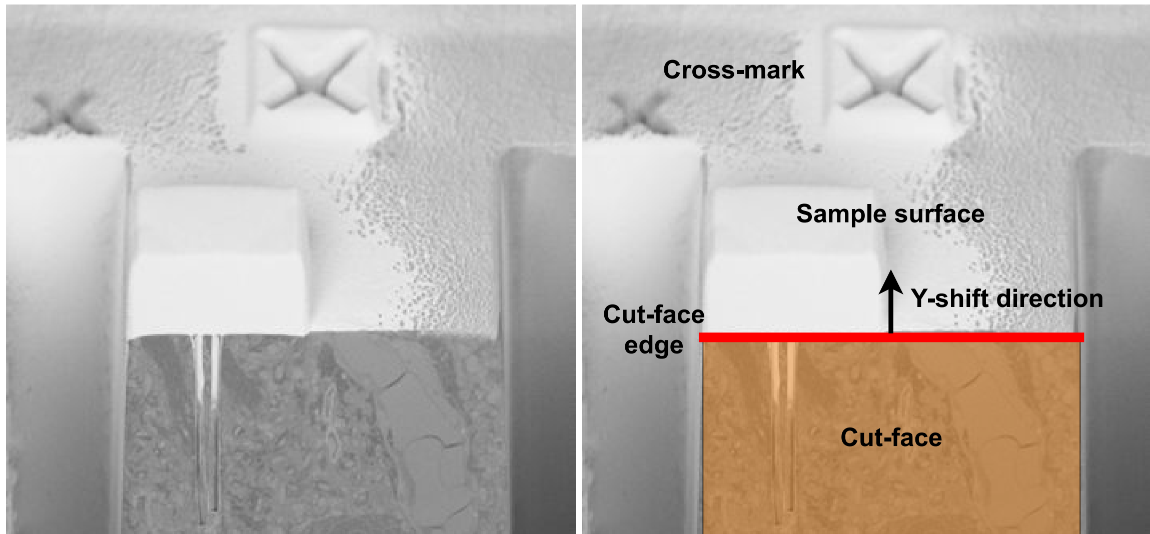

Figure 6.4: Example of a slice image acquired with the SEM from an angle illustrating the Y-Shift SEM slice thickness measurement method principle. The original image **(left)** is augmented with descriptive drawings **(right)**. During the Slice And View process the y-position of the cut-face edge **(red line)** in image shifts in the marked direction **(black arrow)**, because the material layers are sliced off by FIB. Similarly to the Top-Down FIB method, the Y-Shift SEM requires to detect a fixed reference feature to be able to calculate slice thickness values as well.

of the trigonometric functions and the corresponding angles is illustrated in a schematic depicted in Fig. 6.5.

6.3 Implementation of the Measurement Methods

This Section presents techniques for implementing the three slice thickness measurement methods introduced so far, including an algorithm for detecting a horizontal cut-face edge position, utilized in both the proposed methods, and an implementation of the state-of-the-art Chevrons methods. On top of that, an approach for calibrating the microscope magnification is presented at the end.

6.3.1 Need for Reference to Tackle the Image Drift

Besides detecting the cut-face edge position, both the Top-Down FIB and the Y-Shift SEM methods need to detect a second fixed feature in a slice image, to be able to measure a distance between and calculate the slice thickness correctly. This is because the image drift may cause some acquired images to be slightly shifted, and so a single cut-face edge y-position detected in a slice image cannot be taken for the measurement directly.

Luckily, there is the square cross-mark feature present in the slice images, primarily used as an image matching reference during the slicing process, that is detected as the second image feature, having a fixed position. Although its horizontal edges, for example, could be detected by various edge detection techniques, the cross-mark is typically detected as a whole using an internal Thermo Fisher Scientific image matching algorithm. Therefore,

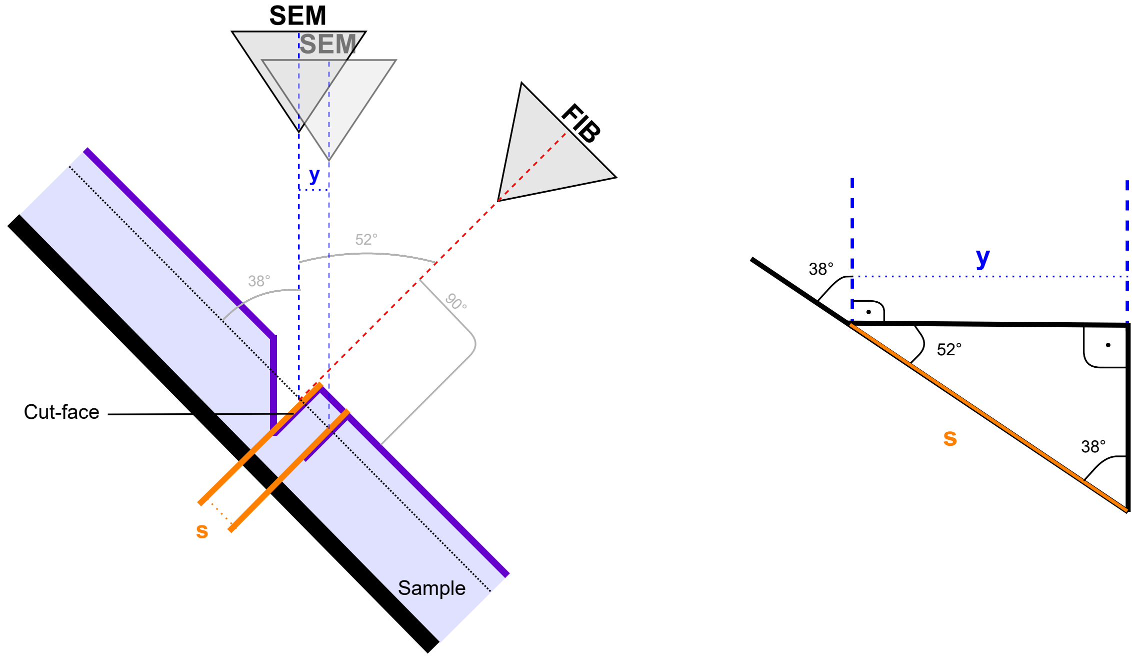

Figure 6.5: A schematic illustrating the cut-face imaging by the SEM from an angle and demonstrating, why do the slice thickness values, measured by detecting image features positions in such acquired images, must be corrected. Assuming that the y **(blue)** represents a difference in two detected cut-face edge positions and the s **(orange)** refers to the actual thickness of a removed material layer, looking at the triangular scheme, obviously, the y value is smaller than the s value. Therefore, to obtain the actual slice thickness, the values measured by the Y-Shift SEM method must be multiplied by a correction factor. Calculation of such correction is presented in Equation (6.1).

an exploration of potential methods for detecting the cross-mark position in image has not been a primary focus of investigation.

6.3.2 Detection of the Cut-Face Edge

The core of both the proposed methods is the detection of the horizontal cut-face edge, changing its position over time due to the slicing process. Observing the slice images presented in Figure 6.2, the detection might seem as a trivial task, because due to a high image contrast caused by the FIB imaging, the the cut-face edge is clearly visible.

Nonetheless, it is not necessarily the case that the position of a cut-face edge is always so clear. Firstly, the edges look differently for different sets of images (as shown in Figure 6.6). One can observe that in some cases the cut-face is not as sharp as the one shown in Figure 6.2. Secondly, the cut-face edge is not always smooth. In the second image of Figure 6.6 the edge profile is quite rough, which makes it harder to identify its exact position.

Including a presence of a natural image drift, caused by positional errors of a beam during the scanning process, resulting in shifts between consecutive slice images, the detection of a cut-face edge position requires developing a robust algorithm resistant to these obstacles.

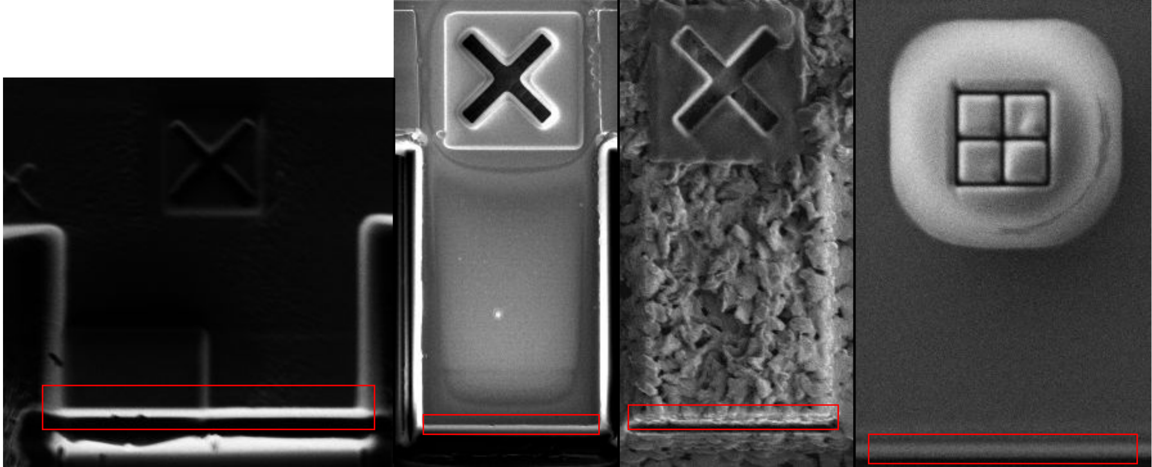

Figure 6.6: Samples of slice images from various datasets acquired for the slice thickness measurement using the Top-Down FIB method. The cut-face edge is marked in each of them **(red rectangles)**. All of them contain a cross mark feature as well, to which the distance from the cut-face edge is measured.

Algorithm for the Cut-Face Edge Detection This thesis proposes an algorithm for the cut-face edge detection, squeezing a 2D slice image into a 1D vector of averaged pixel intensities, which is then averaged again using the moving average and convolved with a Gaussian window. The following paragraphs describe the steps of the algorithm, implemented in the `C#` programming language, more in detail.

At first, an input grayscale image, such as one of the examples from Figure 6.6, is flattened into a one-dimensional vector of pixel intensities. Grayscale pixel values in each image row are averaged into a single integer value, resulting in a column vector with the length of an image height. Subsequently, the vector values are smoothed using a moving average.

To find the edge position, the vector values are convolved with a kernel equal to the second derivative of a Gaussian. Assuming the original series represented as a graph, the values of the resulting series (second derivatives) equal to zero at inflection points, indicating the positions, at which the original graph of averaged pixel intensities changes its curvature. Examples of both vectors, the averaged pixel intensities and the second derivatives, are plotted as graphs in Figure 6.7.

The cut-face edge is usually bright in the image, meaning that the pixel intensities are peaking at its position. Such a peak of averaged intensities is observable in a red graph presented in Figure 6.7. Evidently, there is a significant drop of pixel intensities following its last peak.

Assuming a linear transition from the peaking intensities to the low ones, the cut-face edge position can be determined as a minimum of the blue function (vector of second derivatives). Ignoring the n first and last values of the vector of second derivatives, where n equals to the half of the length of the Gaussian window, symbolizing artifacts, the cut-face edge position can be detected as a global minimum of the second derivatives.

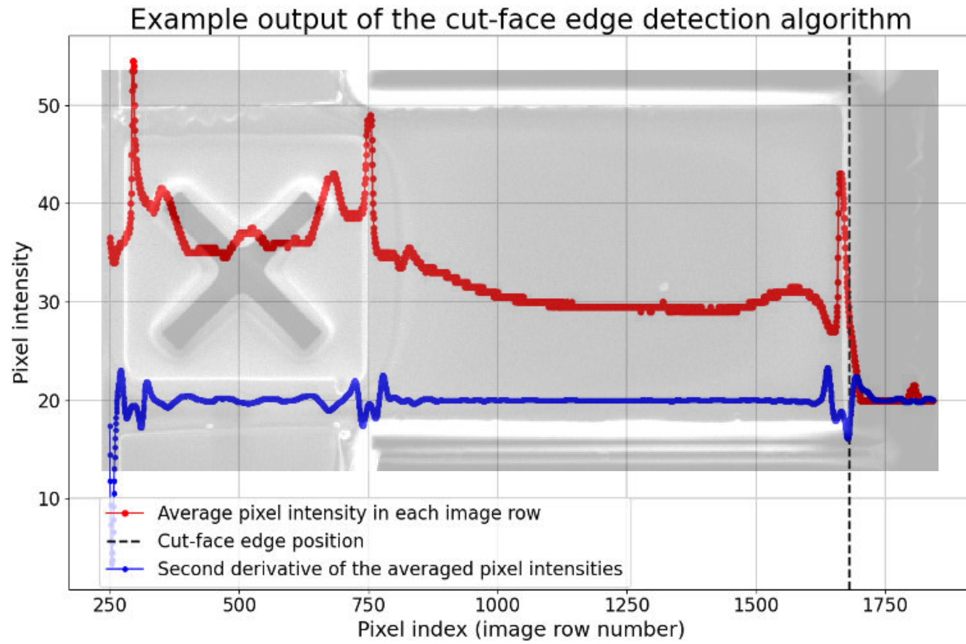

Figure 6.7: An example of a rotated slice image, representing the input of the cut-face edge detection algorithm, overlayed with a graph of vectors of pixel intensities including a detected cut-face edge position, representing the output of the algorithm. The x-axis corresponds to the image row numbers and the y-axis displays the pixel intensities. The **red** function presents the averaged pixel intensities in each image row, while the **blue** one shows their second derivatives. The cut-face edge position, detected as a minimum of the blue graph, is marked by a **black** vertical dashed line. It can be observed that the intensity peaks of the red function correspond to the bright rows of the slice image (such as the cut-face edge).

Alternative Ways of Detecting the Cut-Face Edge Position I also tried to detect the cut-face edge position using more conventional edge detection techniques, by identifying the edge position using the Canny edge detector and refining the detection with active contours. Unfortunately, the cut-face edge profile showed itself to be too rounded and blurred in the image, especially in images acquired by FIB (as shown in Figure 6.8), resulting in the detector was not able to find its position successfully.

6.3.3 Image Features Detection Using the Pattern Matcher

As mentioned, a position of the cross-mark feature in image, from which a distance is measured to a cut-face edge position in both the Top-Down FIB and the Y-Shift SEM methods, is detected using an internal Thermo Fisher Scientific implementation. The algorithm based on discriminative correlation filters [9], referred to as the Pattern Matcher[2], treats images as histograms of oriented gradients and performs template matching with a sub-pixel precision.

[2]Due to the fact that the Pattern Matcher is an internal algorithm owned by the Thermo Fisher Scientific, its implementation cannot be published. Because of this, there is an empty implementation of the Pattern Matcher class attached to the submitted thesis' source code, which is not performing the image matching, but allows to compile the entire edge detection program.

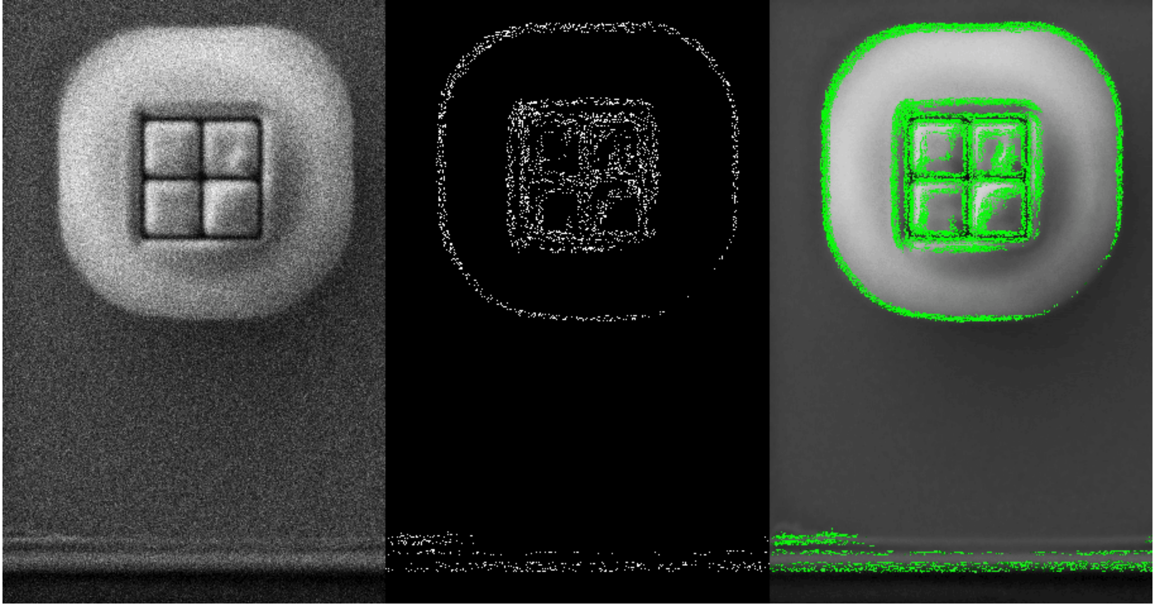

Figure 6.8: An example of an attempt of detecting the cut-face edge position from images acquired by FIB using the Canny edge detector and active contours. On the **left**, there is the original image. The output from the Canny detector, applied to it, then illustrates the binary image in the **middle**. On the **right** there are active contours fit on the detector output and highlighted (green) in the original image. Apparently, the cut-face edge profile is not sharp enough to be able to get more accurate results from the detection.

A minor drawback of using the Pattern Matcher for the cross-mark detection is that it needs a template image for the matching procedure, which means that when developing a detection algorithm using the Pattern Matcher, an area for cropping the template needs to be manually selected. However, this is not a handicap for a use in the Slice And View process, in which the cross-mark feature is being found automatically for controlling the slicing process.

Alternative ways of detecting a cross-mark feature position have also been investigated: First, both the horizontal edges of the cross-mark feature and the cut-face edge detected using the Canny edge detector and, second, the proposed algorithm for a cut-face edge detection. However, they did not prove to be both accurate and robust for the different types of images as the Pattern Matcher is.

Moreover, the Pattern Matcher was tested for the cut-face edge detection too, but did not manage to be as consistent as the algorithm proposed in Section 6.3.2. Due to the fact that the cut-face edge changes its position over time, its profile and shape alter in some slice images. As a consequence, the cut-face edge looks differently from the template image in some slice images, which caused the inaccurate matching results produced by the Pattern Matcher.

6.3.4 Implementation of the Chevrons Method

Unlike the Top-Down FIB and Y-Shift SEM method both implemented in `C#`, measuring the slice thickness using the Chevrons method is implemented in the `Python3` programming language. This is because both the prototyping is faster in `Python3` and there is no aim of integrating the Chevrons method into a Thermo Fisher Scientific production `C#` code base.

Working with the images acquired by the SEM, the chevrons are detected below the cut-face at a defined vertical distance from the cut-face edge. TIn order to find its position as accurately as possible, so that a minimal extra error is introduced into the chevrons detection, it is detected only in the image area between the chevrons, where its position is visually the most clear. Observing a graph of averaged pixel intensities in rows of such an image area, depicted in Figure 6.9, it is evident that a position of the horizontal cut-face edge is distinct enough in this image region.

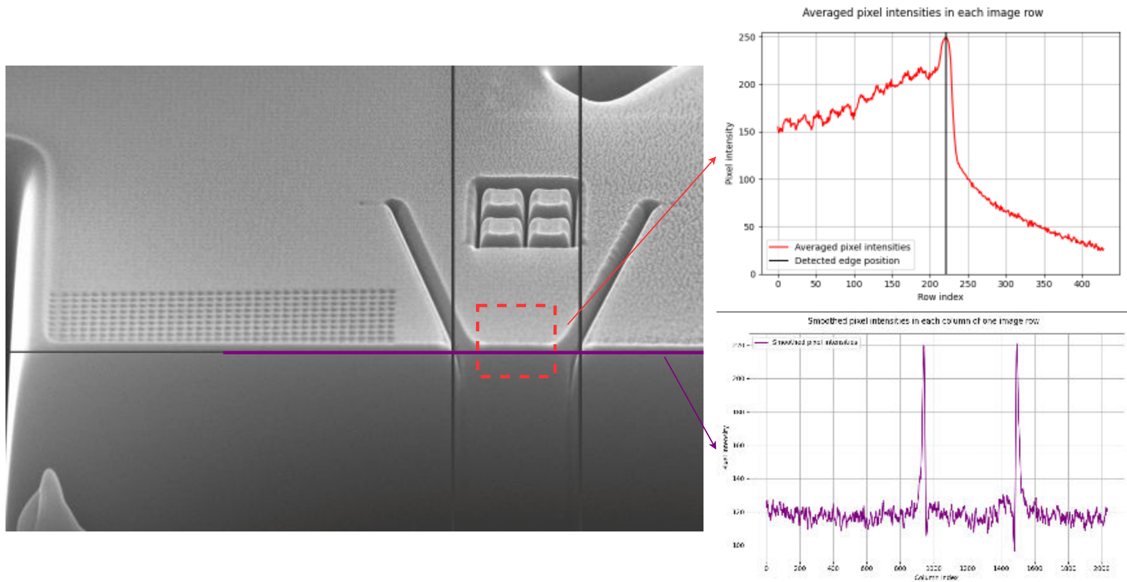

Figure 6.9: An illustration of the implemented chevrons detection. Firstly, a cut-face edge position is found in a sub-image marked by the **red rectangle** in a slice image on the left. The **red graph** on the right presents averaged pixel intensities in each row of the sub-image, showing that the edge position is easily detectable in this image region. The **purple graph** then illustrates pixel intensities in an image row at a defined distance form the detected cut-face edge position. Evidently, there two significant peaks of intensities in the purple graph, indicating the chevrons positions, marked by the two **grey vertical lines** in the slice image.

Knowing the cut-face edge position in each slice image, the chevrons are detected in an image row, which is at a constant distance from the edge in each image of a dataset. Pixel intensities are smoothed by applying a moving average and two local maximums are found, representing bright outer sides of the chevrons on the cut-face (examples of such detected chevrons positions are shown in Fig. 6.9).

Having detected the chevrons positions, the slice thickness values are calculated by the formula in Equation 4.1. Note that the tangent of the angle θ between the two longitudinal marks is known, because the shape of the chevrons pattern was defined before the marks were carved into the sample surface.

6.3.5 Microscope Calibration Requirement

As mentioned in Section 2.2, microscope images, in which features are detected for measuring the slice thickness, might have distorted scale if the magnification of the SEM (or the FIB) is not calibrated precisely. For preventing of measuring false distances in the images, an image of a calibration sample, containing features with standardized dimensions, was acquired each time after a dataset of slice images is gathered.

Looking at the image of such calibration sample in Figure 6.10, it guarantees to contain a square grid of exactly 19.7 lines per millimeter, which corresponds to one line per 50 760.142 nanometers (see Equation (6.2)).

$$\frac{19.7\,\text{lines}}{1\,\text{mm}} \simeq \frac{1\,\text{line}}{0.05076142\,\text{mm}} = \frac{1\,\text{line}}{50\,760.142\,\text{nm}} \tag{6.2}$$

Knowing the actual interval between two lines a similar length is measured manually in the acquired image of the calibration sample, for a comparison. After multiplying such measured distance in pixels by the pixel size of the image, the ratio of these two values, the real length and the measured length, define a correction coefficient, which allows to transform the measured slice thickness values, so that they correspond to the real values. Calculation of such correction coefficient is presented in the following Equation (6.3):

$$Corr = \frac{m \cdot p}{50\,760.142} \tag{6.3}$$

where $Corr$ stands for the resulting correction coefficient, by which the measured slice thickness values must be multiplied (its value is usually ≈ 1.01), m refers to the measured line distance in pixels and p represents the image pixel size in nm.

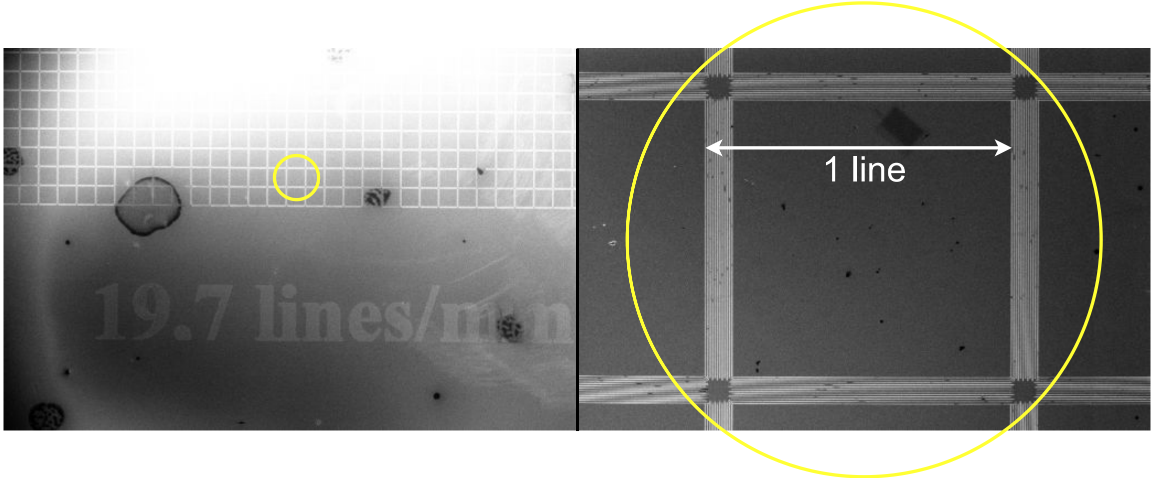

Figure 6.10: Two images of a calibration sample containing a grid of lines, whose mutual distance is guaranteed by a metrological institute. As written on the sample surface **(left)**, there are exactly 19.7 lines per millimeter. The small **yellow circle** marks a square region, in which an interval between two lines can be measured. Observing the yellow image region in a magnified image **(right)**, a distance in pixels between two lines can me measured manually. By comparing the actual distance with the measured one, multiplied by the image pixel size, a magnification correction factor can be calculated.

Chapter 7

Ground Truth Establishment

As declared in Section 5.2, there is no assurance that the state-of-the-art Chevrons method produces real slice thickness values. Unfortunately, the same fact is true for the methods proposed in the previous Chapter 6. Without having a ground truth for the measured values, none of the methods can be properly evaluated or compared.

This Chapter proposes the *Modified Slice And View workflow* serving as a data acquisition method for obtaining the ground truth for the slice thickness measurement and describes its application for evaluating the performance of the individual methods.

7.1 Preparations for the Ground Truth Establishment

Obtaining the ground truth is not a part of the Slice And View process for the 3D sample analysis. A new workflow is proposed, which is based on it, but features a few modifications as, for example, adding a one more preceding stage of creating a referential pattern, whose features will then serve as a reference for the slice thickness values measured by the methods.

It is necessary to highlight that this pattern creation inevitably slows down the entire process, which is, however, only used for evaluating and comparing the performance of the measurement methods. From a user point of view nothing changes – nothing slows down or modifies the original Slice And View process itself. The purpose of this ground truth obtaining process is only to find out how do the proposed methods perform.

7.1.1 Data Acquisition

To be able to use a ground truth for the methods evaluation, it must be somehow obtained. The following enumeration describes the Modified Slice And View workflow for acquiring the data for the evaluation of all the measurement methods:

1. Prepare the sample area for slicing, including a cut-face exposure and placing a referential mark for image matching.
2. Place a special pattern for the ground truth establishment consisting of circular features to be detected, on the sample surface.
3. Slicing: Mill away a layer of material from the cut-face using a FIB, including a removal of some of the circular features.
4. Imaging: Acquire an image of the sample surface using a SEM.

5. Repeat steps (3) and (4) for a defined number of times – slice a number of material layers and generate the same number of images corresponding to them.

6. After acquiring all the images, the resulting dataset is prepared to be used for the ground truth generation and the evaluation of the methods performance.

The Modified Slice And View workflow extends the original one by adding a one more preparation step for placing the referential pattern (2) and apart from that, differs mainly in the imaging step (4), prescribing that the images must be acquired by SEM, because a FIB imaging would have destroyed the pattern of tiny circular features in a just few acquisitions.

7.1.2 Referential Pattern

The referential "dot pattern" consists of small circular features, carved into the planar sample surface by a FIB, of a predefined size and having known distances between each other. It is placed on the sample surface right behind the cut-face edge, so that each time the slicing is performed, there are several dots closest to the cut-face edge being sliced off.

There are six rows of dot features, each of them containing 36 tiny circles, which are not perfectly horizontal, like the cut-face edge is, but slightly tilted. The distances between the individual dot features are in tens of nanometers in both horizontal and vertical directions. Due to the way of using the dot pattern, which is explained more in detail in the following Section 7.2, the objective is having the individual dot features as small as possible and arranged as close to each other as possible. An arrangement of the dots in the pattern is illustrated in Figure 7.1.

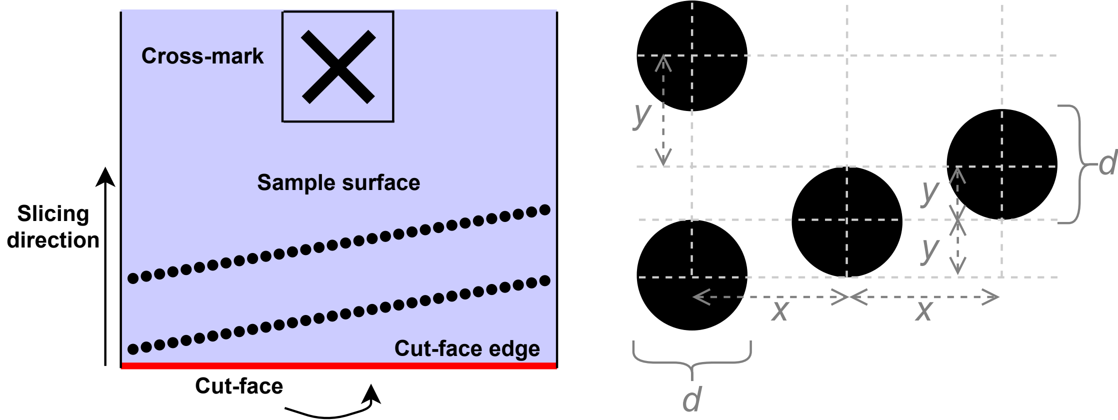

Figure 7.1: Schematic showing two of the total ten rows of a dot pattern arrangement on a sample surface **(left)** and the equal geometry between each of the individual dot features **(right)**. As the slices are continuously removed in the slicing direction **(black arrow)**, the dot features are being milled away from the sample surface. The d as well as the the x and y values are consistent for all of the individual dots and all of the adjacent pairs, respectively. In reality, the y is equal to $\sim$2.08 nm, which means that the subsequently generated ground truth is quantized by this value.

7.2 Using the Referential Pattern for Ground Truth Generation

After placing the dot pattern on the sample surface and obtaining a dataset of slice images for the slice thickness measurement using the Modified Slice And View workflow, it can be used as a ground truth for the measurement. When measuring the slice thickness using the proposed methods as usual, positions of image features are detected, their distance in image is calculated and the resulting slice thickness value is taken as the difference of such distances between two consecutive slice images. In order to measure the slice thickness and evaluate the methods performance at the same time, apart from detecting the image features, the dot features present on the sample surface are detected as well in each slice image.

Due to the fact that the dot pattern is placed near the cut-face edge, in each slice a certain number of dot features are milled away from the sample surface, and thus, as a consequence, do not appear in a slice image, which is then immediately acquired. In other words, for each slice image in the acquired dataset there are less dot features present in slice image $n+1$ than in slice image n. This enables to use the difference in number of dot features remaining on the sample surface between two consecutive slice images as a referential value defining an approximate slice thickness, because the arrangement of dots in the pattern, including the distances between them, is known, as illustrated in Figure 7.2.

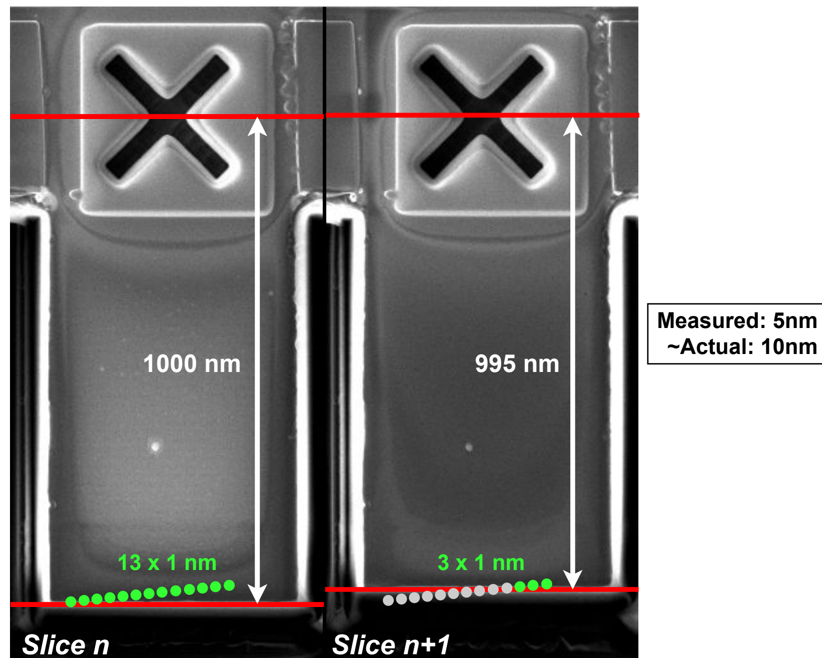

Figure 7.2: Illustration of an example of the measured slice thickness results evaluation shown on the two consecutive slice images from Figure 6.2, augmented with a row of a dot pattern. Referring to the difference of values in the slice images **(white double arrows)**, the measured slice thickness value is 5 nm (after multiplying the difference in pixels by the pixel size value of the images). Assuming that the individual dot features are shifted in the y-direction, marked as "y" in Figure 7.1, by 1 nm (for simplicity), 10 of them were sliced off in the slice $n+1$ compared to the slice n **(gray dots)**, showing that in reality a material layer of about 10 nm thick was removed, correcting the 5 nm prior.

7.2.1 Algorithm for Counting the Dots

The algorithm for detecting and counting the number of dots in a single slice image is implemented in the `Python3` programming language and extensively utilizes functions from the `OpenCV` library [10]. In summary, it fits a non-orthogonal grid to the entire dot pattern and performs a template matching between one representative dot image and each of the individual grid regions to find out, whether it contains a dot or not.

Obtaining the Template Image After enhancing image contrast using histogram equalization and blurring the image with a Gaussian window, the SIFT detector is called to extract keypoints and their descriptors from the image. Thousands of extracted keypoints are then filtered by size and the response value (only the keypoints corresponding to the dots sizes are kept).

To choose the one keypoint representing the area for cropping a template image, a few strongest keypoints are selected (as depicted in Figure 7.3). The assurance that these selected keypoints represent a position of a dot in an input image is obtained by checking that there are low pixel intensity values around its center point and high values in the corners. A template image of a predefined size is then cropped around a keypoint satisfying such constraints.

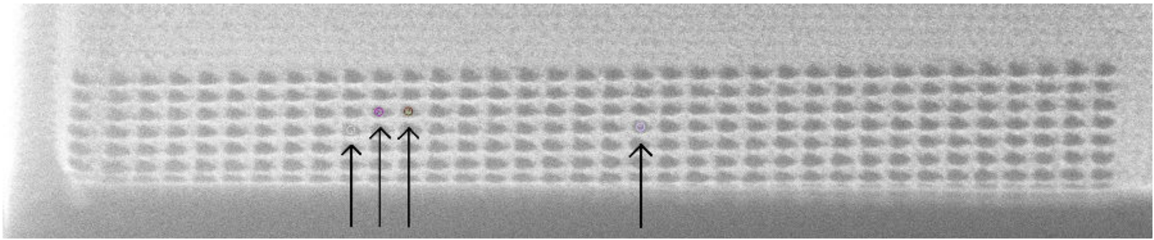

Figure 7.3: An image of a dot pattern showing several keypoints, marked by the colored circles to which the **black arrow** point, satisfying the conditions for being selected as a template for further image matching. Note that the algorithm does not take the entire slice images acquired by the SEM on the input (an example of such a slice image is presented in Fig. 6.9), but processes sub-images of a dot pattern, cropped from the original ones, such as this one.

Detecting Grid Points Once a template image is obtained, it is used for finding the points defining a grid structure. By sliding the template over the entire image, a normalized cross-correlation (NCC) coefficient is calculated at each pixel, with the intention of localizing as many dot regions as possible. By thresholding the response values from the NCC and applying a non-maximum suppression to the remaining locations, represented as bounding boxes, only the most confident matches are kept.

To ensure that there are no redundant or noisy values, the centers of the bounding boxes are clustered and the center points, which are too close to each other are merged together and those, which are too far from any other center points are discarded. The remaining bounding boxes' center points, shown in Figure 7.4 below, are then used for fitting a grid.

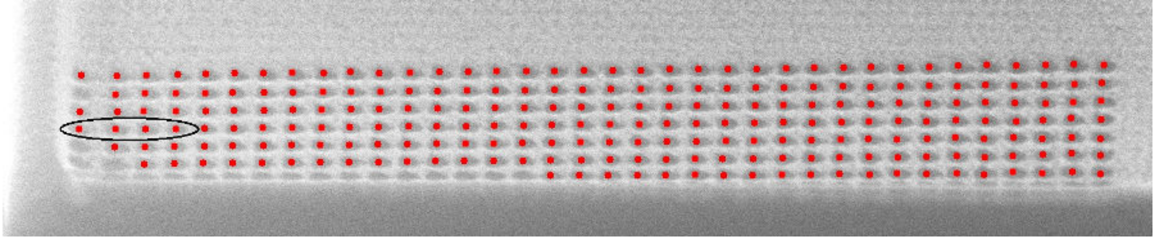

Figure 7.4: An image of a dot pattern showing the detected points, used as the parameters for grid lines fitting. See that the gaps in a horizontal direction between some dots are not uniform **(black ellipse)**. Therefore, fitting a regular grid to the pattern as a whole might not be a precise solution and it is necessary to fit lines to the individual detected dots.

Fitting Grid Lines to Detected Points Typically, there are not enough points detected by the template matching to fit a complete grid of 10 rows and 36 columns, because some dots might have been already sliced off, meaning that the remaining grid lines must be generated by extrapolation. But a majority of lines is fit right onto the points, as follows:

At first, 36 vertical grid lines are being fit. The image is slightly rotated, so that the dots, now represented by the detected points in an image, are vertically aligned. Then, the points' x-coordinates are clustered. As there might not be enough detected points for fitting all the 36 vertical lines, the wanted number of clusters, corresponding to a number of lines to be fit on the points, is unknown. Therefore, the initial step is getting the wanted number of lines by clustering the x-coordinates in different numbers of groups and calculating a silhouette score for each. Knowing the wanted number of lines, the x-coordinates are clustered again, distributing the points in groups, and vertical lines are then fit on each set of points using the weighted least-squares algorithm.

A similar procedure is done for the 10 horizontal lines, except that the detected points are aligned horizontally and clustered by the y-coordinates. Again, the wanted number of clusters is found first and after distributing the y-coordinates into groups, lines are fit on the points. An example of such fitting lines on detected points is illustrated in Figure 7.5

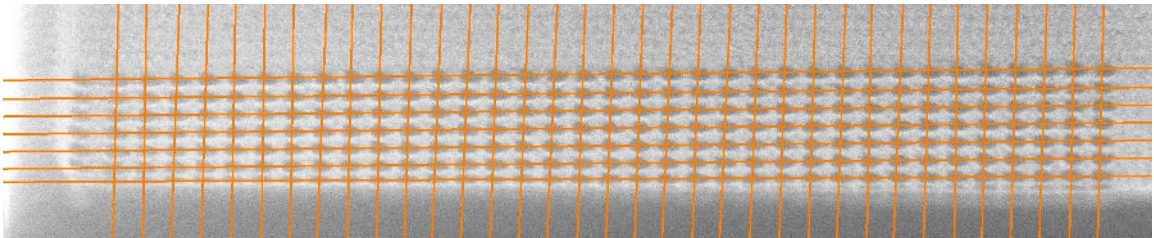

Figure 7.5: An image of a dot pattern depicting grid lines fit on the detected points shown in Fig. 7.4. In this case there is one vertical line on the left and three horizontal lines at the bottom missing to complete the 36×10 grid.

Generating the Remaining Grid Lines In total, 46 lines in total must be fit on a dot pattern image to form a complete grid (shown in Fig. 7.6). If there are some lines missing, they are generated by extrapolating the existing ones.

When estimating the missing vertical lines' parameters, it must be first figured out, which of the 36 wanted ones are actually missing. Center points of the vertical lines al-

ready fit are taken and based on differences between their x-coordinates, gaps are detected, indicating the missing lines. Knowing the x-coordinates of the new vertical lines' center points, the other lines' parameters are estimated from the existing ones.

The missing horizontal lines are usually the bottom ones, corresponding to the area of already removed dots. As each row of the pattern contains 36 dots, there are always enough detected points in the upper part of an image to fit horizontal lines on, meaning that the missing horizontal lines are typically the bottom ones, corresponding to the area of already removed dots. The parameters for the new horizontal lines, a slope and an intercept, are extrapolated from the existing ones, again.

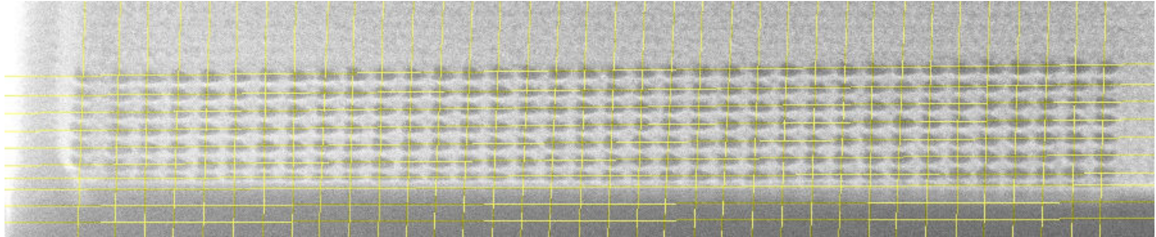

Figure 7.6: An image showing a complete 36×10 grid fit on a dot pattern. The lines intersect at points of expected dot centers in the image.

Template Matching In Grid Regions Once a grid is fit, each of the 360 grid lines' intersections define an expected position of a dot in an image. Around each of the intersection points, a sub-image is cropped, representing a region, in which a dot should be detected using the template matching.

Note that the template image, already cropped around a keypoint detected by the SIFT, has a 15% smaller size compared to the individual grid region crops, so that it can slide over them, calculating a NCC for each template image – grid region pair and producing a matrix of response values.

For each of the grid regions, a similarity score, representing the measure of how much a template image with a dot matches a cropped grid region image, is set as a maximum value from the NCC response matrix. Figure 7.7 shows a comparison of grid region images very similar to a template image, having high similarity scores, and images with low similarity scores corresponding to the already removed dots.

Thresholding the Scores And Counting the Dots Having a set of similarity scores, each representing a likelihood of presence of a dot in a grid region, the last step remaining to be able to count the number of dots in a slice image is splitting the scores in two groups – dots and non-dots. By treating the set of scores as a graph of values sorted by distance of the individual dots from the cut-face edge, starting at the top-right and ending at the bottom-left, a threshold is found for each slice image as follows:

Firstly, the scores are smoothed by a moving average and split in two groups by a global minimum value. Looking at the progression of scores in a graphical representation in Fig. 7.8, one can observe that it typically starts with a constant part of high scores, representing the grid regions extracted from the top rows of the pattern containing dots, followed by a significant drop of scores near the cut-face edge, where the slicing is done, and ending with another constant part of lower scores, corresponding to a bottom part of an image depicting the cut-face with no dots. This means that the actual threshold

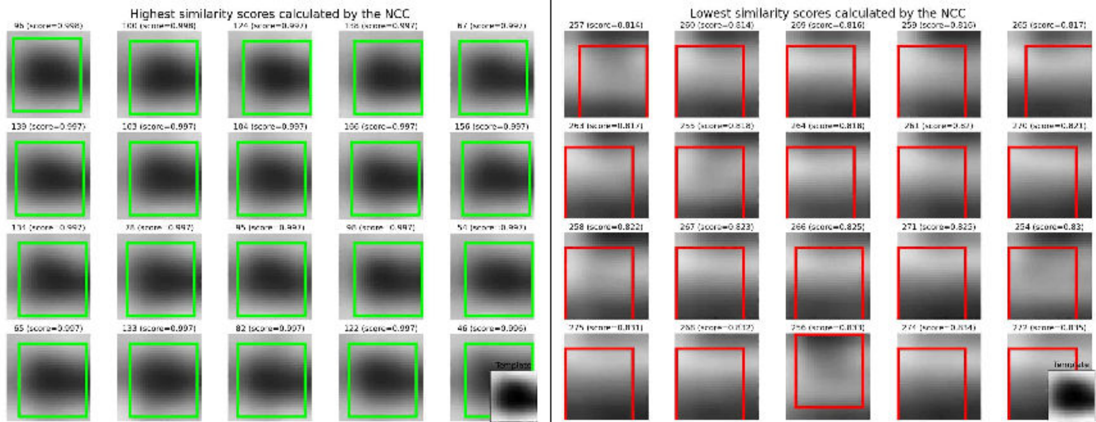

Figure 7.7: A comparison of similarity scores calculated by NCC for the individual grid region image crops. On the left there are image crops marked as the most similar ones to the template image (depicted in the bottom-right corner) and on the right there are the least similar ones, sorted by the score value from top-left to bottom-right. Each region crop label contains an index, corresponding to its topological position in the pattern, an a score value. The green and the red squares mark the image area, which produced the highest response score when sliding the template over the image and calculating the NCC.

value lies somewhere between the left constant part of high scores, surely representing the dots present, and the right constant part of lower scores, corresponding to the noise in the bottom part of an image. Likewise, splitting the scores in such two groups ensures that the threshold value should definitely lie in the first group, somewhere at the steep part of the scores function, corresponding to the cut-face edge area.

Based on the intuition that the threshold value lies between the two constant parts, each group of scores, created by the global minimum split, is searched for such flat region. The constant part in the first group of scores is set to start with the very first dot (indexed from the most top-right one to the most bottom-left one) and ends with a first local maximum point detected on the left from the steep part of the scores curve. Analogously, the end of the flat part in the second group of scores ends at an index of the last grid region, surely corresponding to an image crop of an already removed dot, and starts at the first score value differing too much from all the previous ones, when taking values one-by-one from the end to the left.

Note that in a first few slices of a dataset a majority of dots is typically not sliced off yet, meaning that there are just a few grid regions' scores representing the second group. In order to detect a constant part in the second group of scores more accurately, one or two additional horizontal grid lines are generated at the bottom of an image, allowing to create more grid regions with low similarity scores.

Having both of the flat parts located, an average score is calculated for each of them and the resulting threshold value is set in the middle of these parts, which corresponds to a point on the steep part of the scores curve. Knowing a threshold value, the index of a thresholding grid region, representing a dot, is set to the one with the score value closest to the threshold. Finally, all the grid regions with an index lower than the thresholding one are counted as the dots still present on the sample surface (all the green dots, looking at the image in Figure 7.9), and the regions with indexes beyond the threshold are marked as the dots, which were already sliced off.

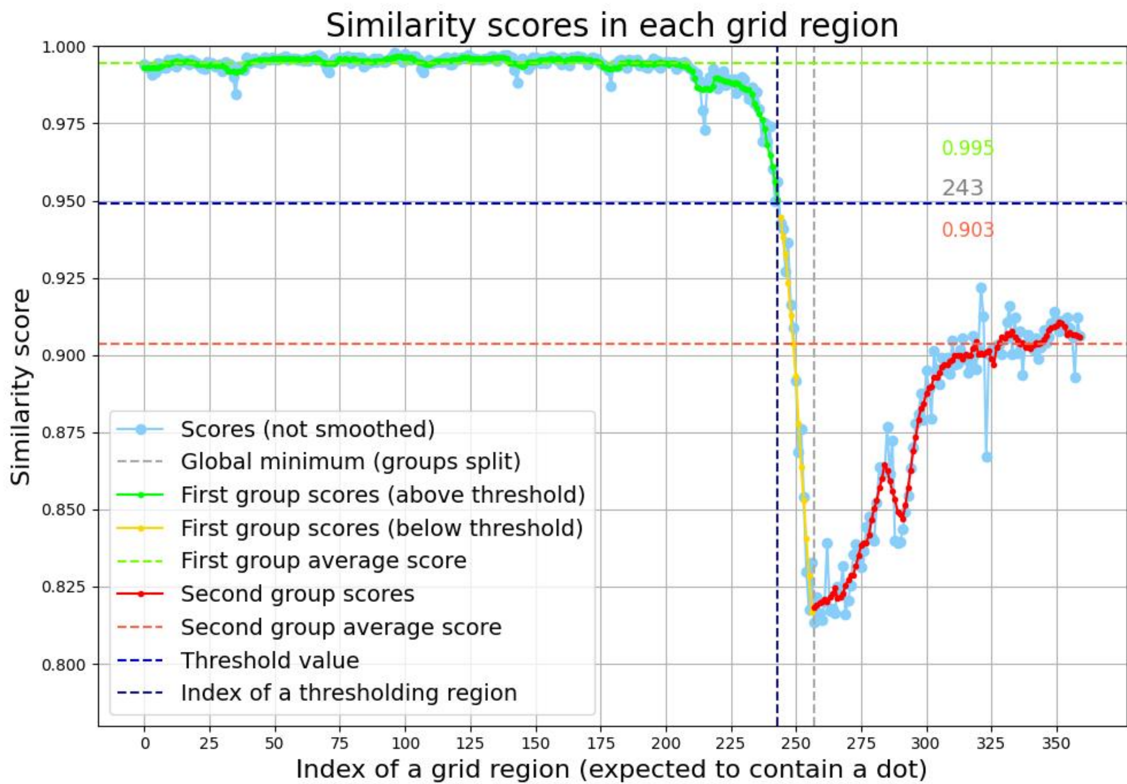

Figure 7.8: An example of similarity scores **(blue)** for each of the 360 grid regions plotted as a graph, sorted by positions of dots in the pattern, starting at the top-right and ending at the bottom-left. The **green** and **yellow** curves represent the averaged scores from the first group (after splitting all the scores by the global minimum) and the **red** curve represents the scores of the second group. The **green** and **red vertical dashed lines** represent the detected borders of both flat parts and the **horizontal lines** of the similar colors mark the average score value in each group.The **gray dashed lines** then represent the threshold value and the index of a thresholding dot region. All the green values are counted as dots present in the image.

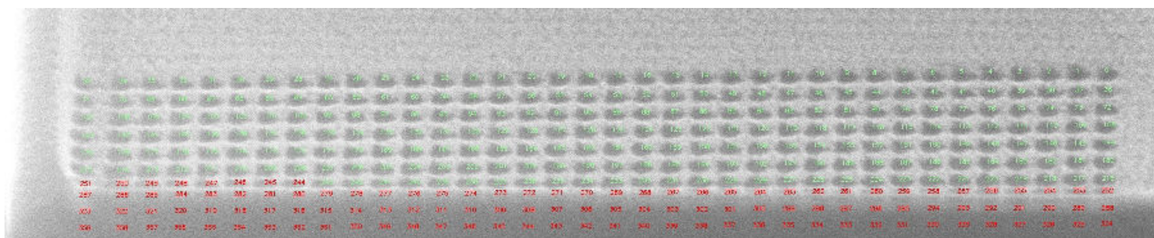

Figure 7.9: A visualization of dots, which were counted as the still present ones on the sample surface **(green)** and those, which were marked as the already removed ones **(red)**. The dots indices **(green and red numbers)** match the topological positions of the individual dots in the pattern, sorted from the top-right to the bottom-left. This image corresponds to the graph in Fig. 7.8, except that the red dots in this example correspond to both the yellow and red scores plotted in the graph.

7.3 Manual Ground Truth Alternative

For a comparison to the referential slice thickness values measured by the algorithmic ground truth obtaining method, I developed a manual alternative. Working with the same source images as the algorithmic method does, a distance from a center of the most top-left dot in a pattern to the visually estimated cut-face edge position is measured by hand (as illustrated in Figure 7.10). By multiplying the measured distance in pixels by the image pixel size and the constant compensating the non-perpendicular view angle of the SEM, a slice thickness value is calculated.

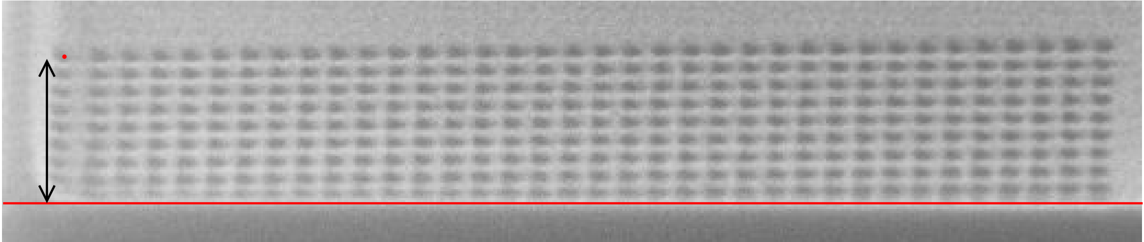

Figure 7.10: An image of a dot pattern illustrating the principle of obtaining ground truth values for the measurement manually. In each such cropped image of a dataset acquired using a SEM (the same source images as uses the proposed ground truth obtaining algorithm) positions of the top-left dot's center **(red dot)** and the cut-face edge **(red line)** are both marked by hand and their distance **(black arrow)** in pixels is measured.

Chapter 8

Experimental Results

This Chapter provides a closer look on the datasets of slice images acquired for developing the algorithms for the image feature detection and evaluating the performance of the individual methods. After that, the experimental results are presented and discussed and the individual measurement methods are compared to each other.

8.1 Acquired Data for the Experiments

This Section presents three datasets, on which all the measurement methods introduced in this thesis were evaluated, describes the process of their acquisition and discusses the characteristics of the acquired images.

8.1.1 Data Acquisition Workflow

For each of the three datasets, labeled as Dataset 1, Dataset 2 and Dataset 3, source images for all the three measurement methods (Chevrons, Top-Down FIB and Y-Shift SEM) and both the ways of obtaining the ground truth were acquired in a single image acquisition session, in order to the have all the images from a dataset gathered under equal microscope conditions. The process of acquiring a dataset for evaluating all the methods is similar to the Modified Slice And View workflow, presented in Section 7.1.1, but extends the preparation step by placing image features on a sample surface, required by the other methods, as well. In addition, there are two imaging steps (for both the SEM and the FIB) instead of just one. A schematic in Figure 8.1 shows an arrangement of all the features and imaging areas on a sample surface for acquiring a complete dataset for the methods evaluation.

8.1.2 Characteristics of the Image Datasets

I acquired three datasets for the measurement, each consisting of slice images acquired by SEM and the same number of images acquired by FIB. Both the Datasets 1 & 2 consist of 13 images used for the actual measurement and the Dataset 3 contains 12 of them. In all cases, the expected slice thickness was set to be 40 nm, which was chosen as an acceptable trade-off between the total number of slice images in a dataset and the expected number of dots removed each slice, which is aimed to be as high as possible, so that the quantization, caused by the 2.08 nm distances between two dots in the y-direction, adds as minimal error as possible to the measured ground truth values.

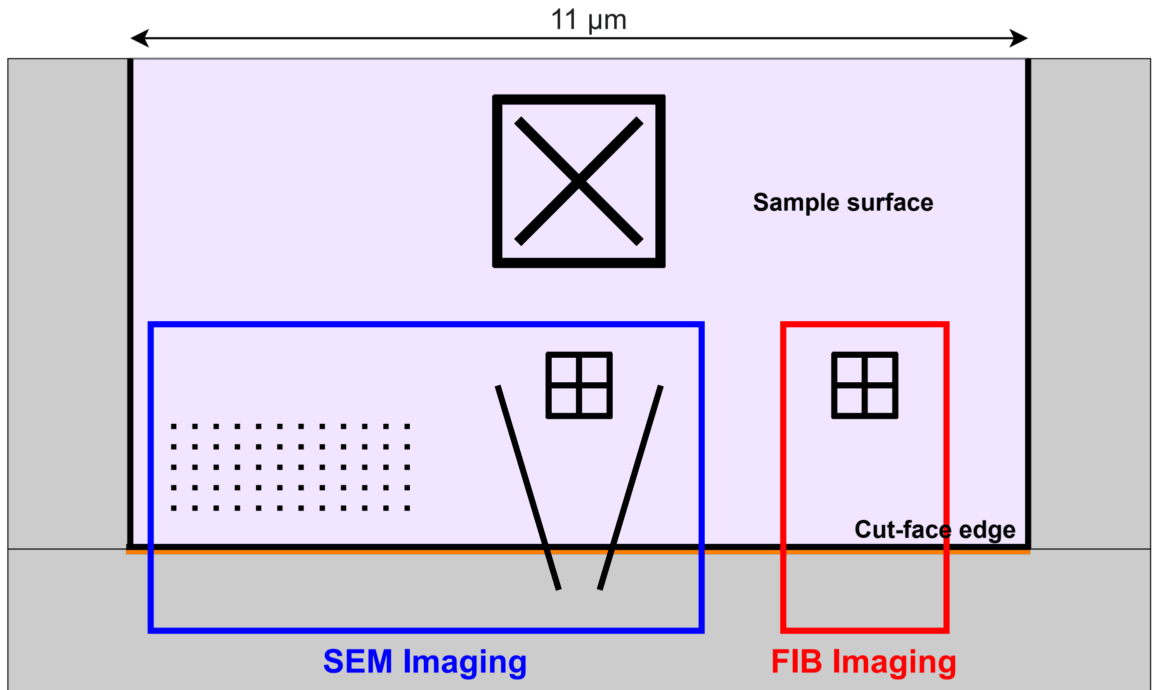

Figure 8.1: A schematic of a top-down view on the sample surface. After performing all the preparation steps, the area, where the images are being acquired is $11\mu m$ wide, meaning that the size of the individual features is in the order of micrometers. There is a dot pattern in the **bottom-left** corner, and the chevrons and a referential cross-mark feature for the Y-Shift SEM method in the **middle**. All these features are acquired in a single SEM image **(blue rectangle)**. On the **right** there is another referential cross-mark feature placed, being detected by the Top-Down FIB method, requiring a separate FIB imaging **(red rectangle)**. In each images of the resulting dataset (in both the SEM and FIB subsets of images) a cut-face edge must be present as well.

Image samples from all the three datasets are presented in Figure 8.2. Looking at them, one can observe that the images acquired by SEM in the Dataset 1 and the Dataset 2 are relatively similar to each other and slightly different from the images in the Dataset 3 at the same time.

Images in both Figure 8.3 and Figure 8.4 show some specifics of the acquired images. In Fig. 8.3 the a natural image drift is observable, as well as differences in image quality caused by an imperfect focusing of the electron beam. Figure 8.4 shows an example of an effect of focusing a beam of the heavy ions on the same spot for a longer time period.

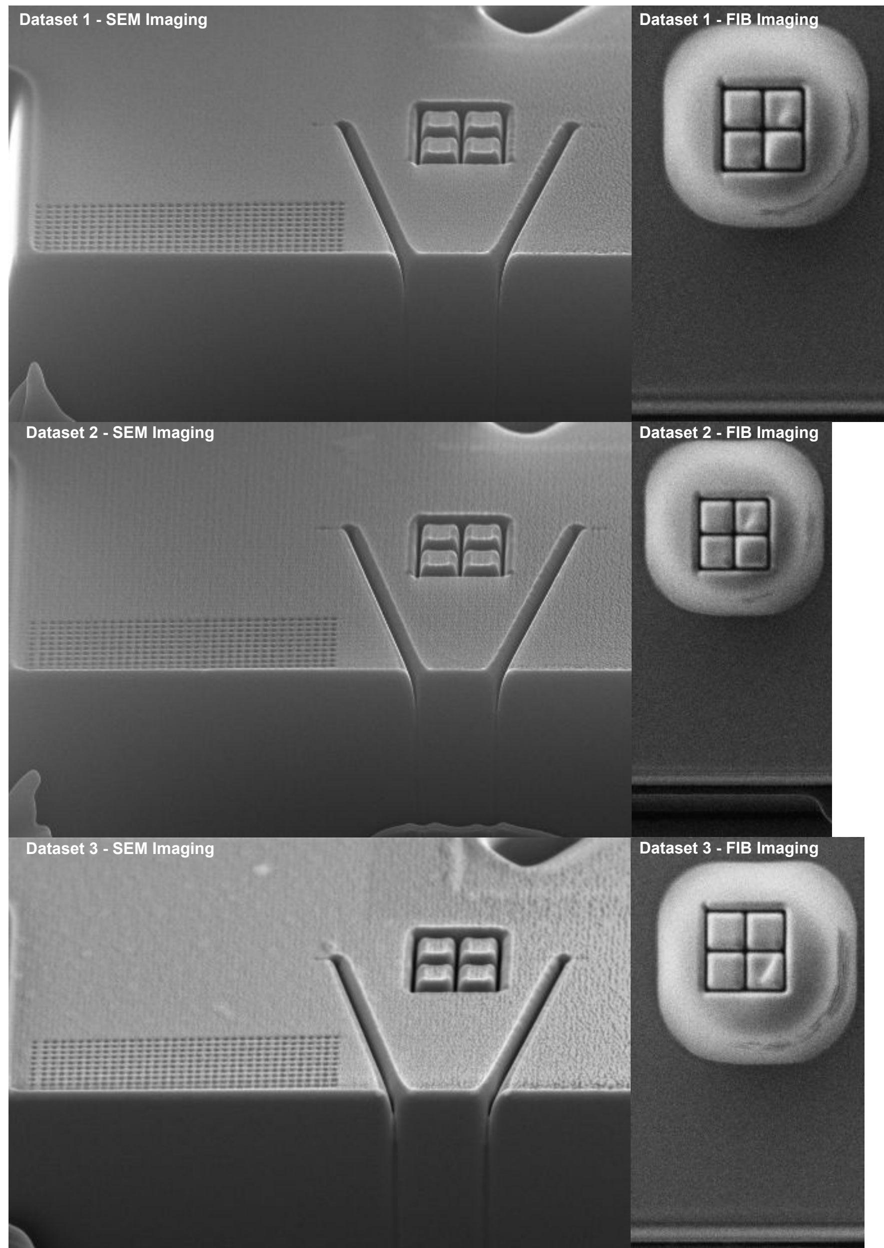

Figure 8.2: First slice images of both the SEM imaging subset and the FIB imaging subset from all the three datasets. In the images acquired by SEM **(left column)** there are the dot pattern for the ground truth obtaining method, the chevrons and a cross-mark feature for the Y-Shift SEM. It is evident that a majority of the dots were not sliced off yet. The other referential cross-mark feature for the Top-Down FIB, present in in the images acquired by FIB **(right column)**, is placed in the middle of a bright protective layer of deposited tungsten, making the cross-mark more resistant to the irradiation of the ion beam. In all the images, the cut-face edge is visible as well. One can observe that it is more blurred in the images acquired by FIB.

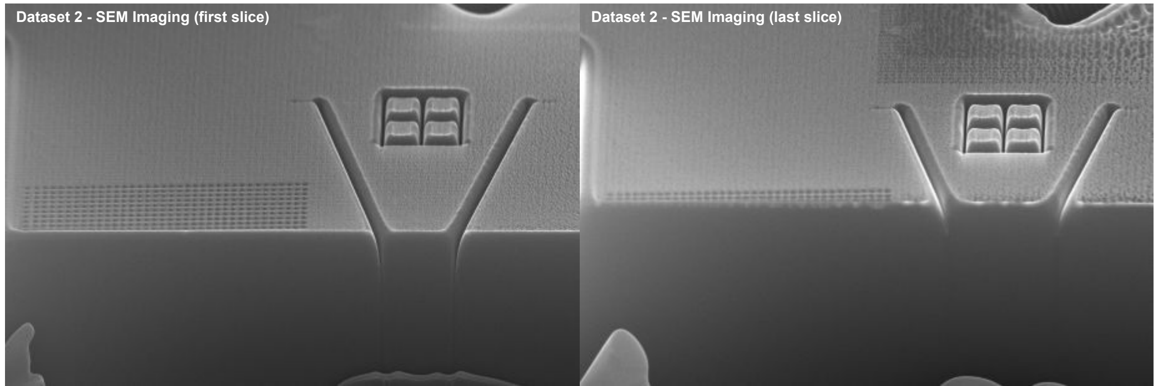

Figure 8.3: Examples of a first **(left)** and a last **(right)** slice image of the SEM imaging subset of the Dataset 2. Observing the images, clearly to see that the cut-face edge position is closer to the cross-mark (having a fixed position) in the last slice image, because many material layers were removed since the time the first slice image was acquired. Evidently, many rows of dots were removed between the first and last slice as well. An interesting thing to see is that in the last slice image the dots are more blurred compared to the ones in the first slice image. Unfortunately, for some images of the dataset, such as the one above, the electron beam was not perfectly focused on the dot pattern during the image acquisition.

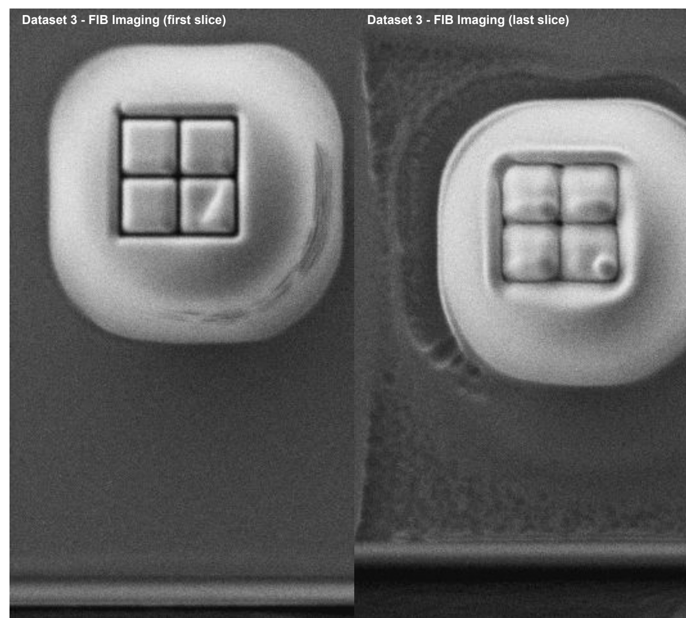

Figure 8.4: Examples of a first **(left)** and a last **(right)** slice image of the FIB imaging subset of the Dataset 3. It can be seen that the sample surface, including the cross-mark is much more deformed in the last slice image than in the first one, which clearly demonstrates the destructive effects of the ion beam, slowly "melting" the area being exposed to it, even though the beam current was set to be minimal during the imaging activity. Besides, it as apparent that the cross-mark feature is not perfectly centered in the last slice image, as it is in the first one, which is caused by the image drift, already mentioned in Section 2.2.2.

8.2 Evaluation of the Methods

This Section presents the experimental results showing the performance of the individual methods, comparing them and discussing both their accuracy and precision. The methods were evaluated on all the three datasets presented in the previous Section 8.1. According to that, a majority of figures depicting the results in this Section consists of three similar images, one for each dataset. The metric used for measuring the error of the individual methods is either the absolute difference between the slice thickness values or, in some cases, the mean of these absolute differences.

8.2.1 Accuracy

When comparing the methods to the ground truth obtained by the algorithm, the Chevrons method and the Top-Down FIB method give the most consistent results, as the difference of values measured by the Chevrons method from the ground truth is between $3 - 5$ nm for all the three datasets, and for the values measured by the Top-Down FIB the difference is between $1.8 - 3.8$ nm, referring to the matrices shown in Figure 8.6.

Furthermore, Figure 8.5 shows the absolute difference between the ground truth values determined by the algorithm and the ones measured by the other methods. One can observe that both the lines representing the Chevrons method and the Top-Down FIB give a minimal error. However, there is at least one error value differing by $\sim$10 nm from the the ground truth for the Chevrons method, and none for the Top-Down FIB method, for each dataset. Alongside the fact that the Top-Down FIB has the lowest mean of absolute differences from the ground truth, it can be labeled as the most accurate one from all the three methods evaluated on the available datasets.

The possible reasons of the Y-Shift SEM method producing unstable results and being less precise compared to the other two methods are discussed in the following Section 8.2.2.

8.2.2 Comparing the methods behaviour

The matrices in Figure 8.6 show the means of absolute differences of measured values between each pair of methods, including the ground truth obtaining ones, for each dataset.

At first sight of the cell colors in the matrices, there is no doubt that for the Datasets 1 & 3 the most outlying values produced the Y-Shift SEM method and for the Dataset 2 it was the manual ground truth obtaining method. For the images from the Dataset 1 the values measured by the Y-Shift SEM differ from all the other methods even by more than 13 nm in average.

Observing the measured slice thickness values plotted as graphs in Figure 8.7, the trend that the Y-Shift SEM method measures unstable values for the Datasets 1 & 3, but not for the Dataset 2 is even more obvious, than in the matrices in Fig. 8.6. This might be caused by the characteristics of the individual Datasets. However, the images in the Datasets 1 & 2 are more similar to each other than to the ones in the Dataset 3, which is contradictory to the observed results. Probably, the Y-Shift SEM is highly sensitive to the actual data and the cut-face edge profile in them, which might be the most consistent in the Dataset 2.

It is remarkable that the differences are not that huge for the Top-Down FIB method too, which works on a similar principle, detecting the same two features in images. The results of the Top-Down FIB are more similar to the Chevrons method, having a mean of absolute differences under 5.2 nm for all the three datasets, as shown in Fig. 8.6.

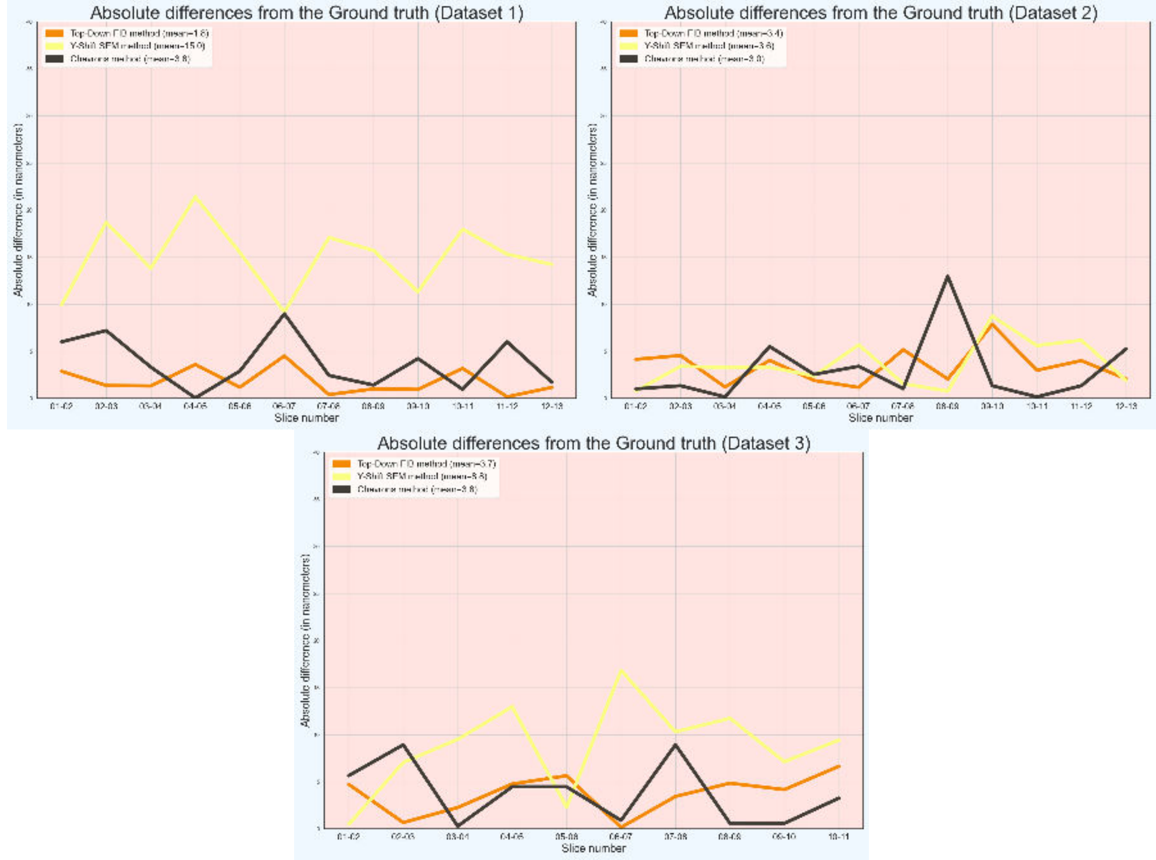

Figure 8.5: Graphs of absolute differences in measured slice thickness values between a ground truth obtained by the algorithm and the measurement methods, one for each dataset. In each graph, the x-axis presents the slice numbers and the y-axis shows the error from the ground truth, in nanometers. Values measured by the individual methods are plotted as lines, each with a different color. In the legend depicted in the top-left corner there are means of summed absolute differences for each method. Note that the graph for Dataset 3 shows results for only 11 slices, not all the 12. The first slice of the dataset was excluded from the comparison, because of having an anomalously low ground truth value.

Comparing the ground truth obtaining methods As for the values measured manually as the ground truth, they fluctuate the most for the Dataset 2, but deviate from the expected 40 nm average quite much for the other two datasets as well (referring to the slice thickness values presented in Fig. 8.7). Such a performance indicates that the ground truth values determined manually might not be an authentic reference for the slice thickness values measured by the other methods. On the other hand, the reason why did the algorithmic ground truth obtaining method measured an extremely low value in the first slice of the Dataset 3 remains unclear even after a deeper investigation of the individual measured values.

Observing the matrices in Fig. 8.6, it can be seen that the means of absolute differences in measured slice thickness values are high between the ground truth values measured by the algorithm and those determined manually: 6.17 nm, 8.60 nm, 3.40 nm. This fact indicates that at least one of the two methods for obtaining ground truth produces inaccurate values. It cannot be decided with an absolute certainty from the available results which one does,

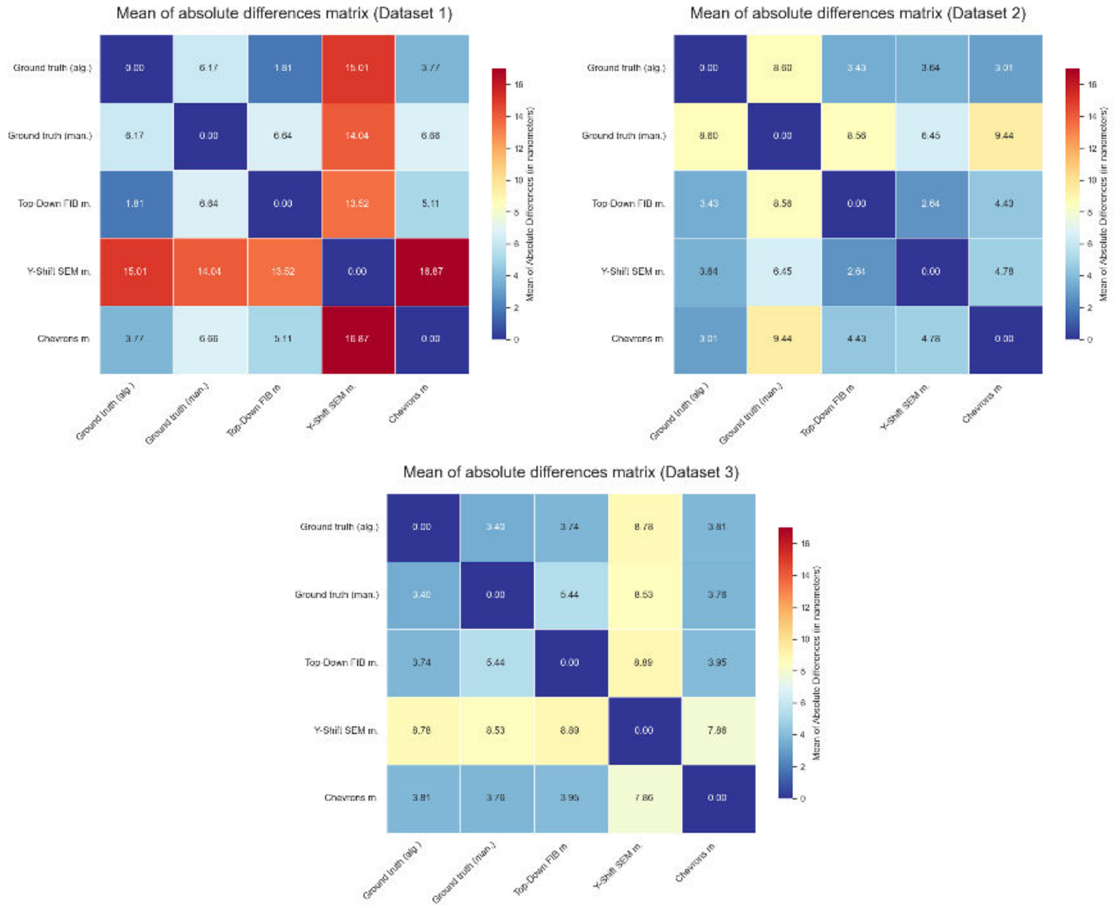

Figure 8.6: Symmetric matrices of means of absolute differences of measured slice thickness values between each pair of all the methods including the ground truth obtaining ones. There are five rows and five columns in each matrix, one for each method. The colors of the cells reflect the mean values, expressed in nanometers, as follows: the lower error value, the more **blue**, the higher error value, the more **red** (corresponding to the scale on the right). Clearly, the slice thickness values measured by the Y-Shift SEM method for the Dataset 1 differ the most from all the others in average.

but a notable disadvantage of the manual alternative is that it obtains slice thickness values by measuring distances in image by hand, which is accurate to at most a pixel. On the other hand, the ground truth obtained by the algorithm is quantized by the difference between the y-positions of the adjacent dots in the pattern.

Nevertheless, despite such a quantization the measured values are relatively stable (referring to the graphs in Fig. 8.7). Moreover, taking into account the fact that the algorithmic method works on a completely different principle compared to the other methods detecting a cut-face edge position, which does the manual alternative detect too, probably, the ground truth obtained by the algorithm is closer to the actual slice thickness compared to the manual alternative.

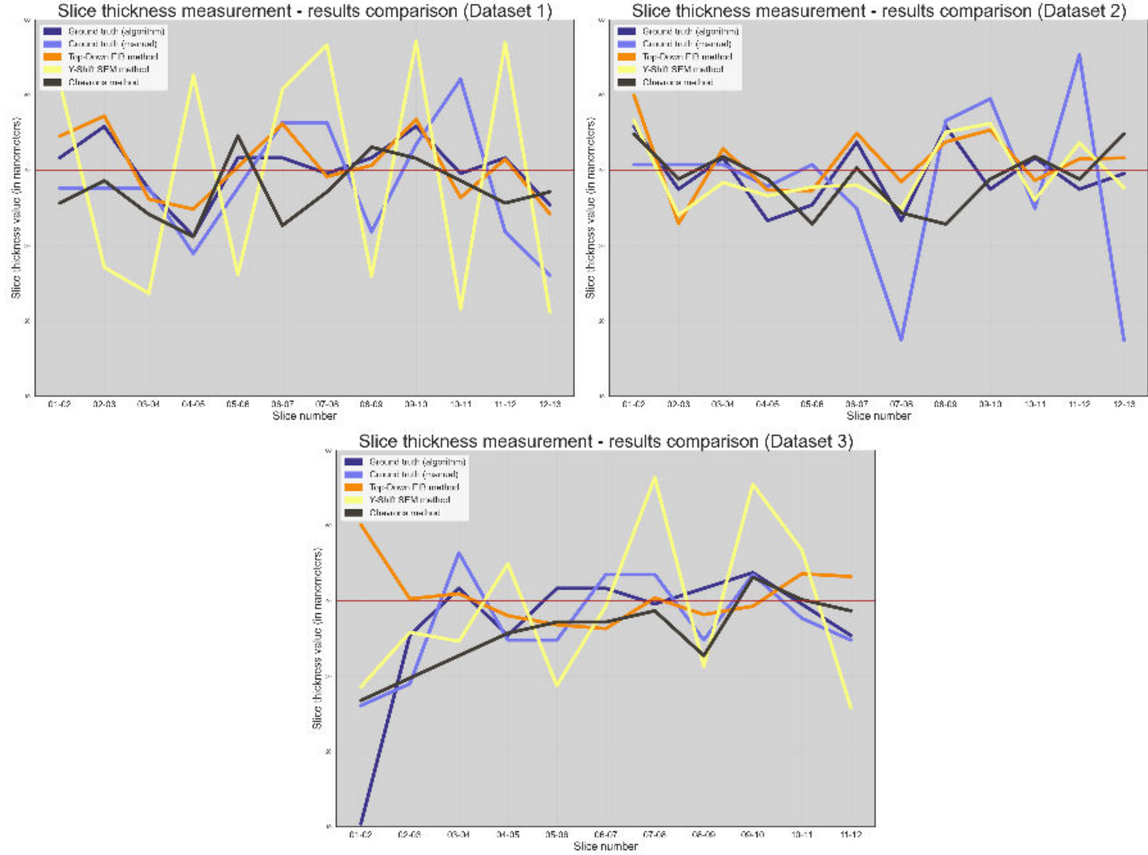

Figure 8.7: Graphs of measured slice thickness values for each dataset. In each graph, the x-axis presents the slice numbers and the y-axis shows the measured slice thickness values in nanometers. Values measured by the individual methods are plotted as lines, each with a different color, and there is a **dark red** horizontal line, depicting the expected 40 nm value as well. Evidently, the measured values produced by the Y-Shift SEM method **(yellow)** fluctuate the most for both the Dataset 1 and the Dataset 3. For the Dataset 2 the manual alternative of the ground truth obtaining method **(light blue)** gives the most unstable results. Lastly, the proposed algorithm for counting the dots **(dark blue)** measured an extremely low thickness in the first slice of the Dataset 3.

8.2.3 Overall statistics

Finally, Table 8.1 shows the overall statistics, a mean a standard deviation for all the measurements performed by each of the methods. None of the measured mean values are more than 2 nm away from the expected average of 40 nm, except the Chevrons method, whose mean values are slightly lower. I tried to investigate why it is so by analysing the measured slice thickness values and by checking the correctness of the implementation, but made no discoveries. Acquiring more datasets might help to answer this question.

The mean values of the algorithmic ground truth obtaining method alter between 39.4 nm and 40.3 nm in all the three measurements performed, indicating that the real slice thickness might be actually close to the expected thickness of 40 nm.

By observing the standard deviations, the highest ones belong to the Y-Shift SEM method followed by the ground truth values measured manually. Taking into account the

results seen in Fig. 8.5, Fig. 8.6 and Fig. 8.7, this is an expected outcome. In contrast, the other methods, the Top-Down FIB, the Chevrons method and the ground truth determined by the algorithm maintain their standard deviations around 4 nm, making them the more stable measurement methods compared to the other two.

Dataset	Ground Truth (A.)	Ground Truth (M.)	Top-Down FIB M.	Y-Shift SEM M.	Chevrons M.
1	40.278 nm ± 4.103 nm	38.131 nm ± 7.794 nm	40.684 nm ± 4.690 nm	39.305 nm ± 15.892 nm	37.517 nm ± 4.063 nm
2	39.410 nm ± 4.393 nm	38.100 nm ± 11.276 nm	41.242 nm ± 4.565 nm	39.600 nm ± 4.519 nm	39.095 nm ± 4.071 nm
3	39.583 nm ± 3.106 nm	39.583 nm ± 5.603 nm	39.410 nm ± 2.390 nm	39.951 nm ± 10.667 nm	36.598 nm ± 3.980 nm

Table 8.1: A table presenting mean and standard deviation values measured for each of the five methods **(columns)** in each of the three datasets **(rows)**.

Chapter 9

Conclusion

In this thesis two new methods for measuring the thickness of material layers removed from a sample in an electron microscope, which are more practical compared to the existing one, were presented. For implementing the proposed methods a new robust algorithm detecting the horizontal cut-face edge was introduced. In addition, a method for obtaining the ground truth for the measured results, allowing to compare the other methods and evaluate their accuracy, was presented, including an implementation based on detecting tiny circular features in image.

I created three datasets for evaluating the individual methods, each consisting of two subsets of 12–13 slice images. The experimental results show that the Top-Down FIB, one of the proposed methods, measures consistent values, which are close to the expected slice thickness. Also, when compared to the ground truth, it showed a slightly better performance compared to the existing Chevrons method. Furthermore, the algorithm for counting the tiny circular features in image appears to be usable for obtaining the ground truth for the measurement, as it produced more stable results than the alternative method, manually annotating the data.

To draw clearer conclusions from the results, it is necessary to evaluate the methods on more datasets of images. The process of acquiring images for all the measurement methods at once, including the ground truth obtaining method, was the most challenging part of this project, as it was hard to place the 2 nm circular features on a sample surface precisely, under available microscope conditions.

Nevertheless, I still believe that the goal of this thesis was achieved, as there is a new slice thickness measurement method, which is more practical than the existing one and shows a comparable performance at the same time, and an approach of obtaining the ground truth for the measured values. In the future, first of all, I am planning to acquire more datasets of images. Once having the data, the performance of all the proposed methods can be further improved and the experimental results might give clearer conclusions.

The work of this thesis was presented at the Excel@FIT 2023 student conference and was awarded by both the expert committee and Edhouse company.

Bibliography

[1] Xu, M., Liu, J., Sun, J., Xu, X., Hu, Y. et al. Optical Microscopy and Electron Microscopy for the Morphological Evaluation of Tendons: A Mini Review. *Orthopaedic Surgery*. 2020, vol. 12, no. 2, p. 366–371. DOI: 10.1111/os.12637. Available at: https://onlinelibrary.wiley.com/doi/abs/10.1111/os.12637.

[2] Alberts, B., Johnson, A., Lewis, J., Walter, P., Raff, M. et al. *Molecular Biology of the Cell 4th Edition: International Student Edition*. Routledge, 2002. ISBN 9780815332886. Available at: https://books.google.cz/books?id=ozigkQEACAAJ.

[3] Ul Hamid, A. *A Beginners' Guide to Scanning Electron Microscopy*. January 2018. ISBN 978-3-319-98481-0.

[4] Goldstein, J., Newbury, D., Echlin, P., Joy, D., Lyman, C. et al. Scanning Electron Microscopy and X-ray Microanalysis. In:. January 2003, chap. Specimen Preparation of Polymer Materials, p. 565–590. DOI: 10.1007/978-1-4615-0215-9_12. ISBN 978-1-4613-4969-3.

[5] Petranova, V., Koudelka, P. and Valach, J. Determination of Drift distortion in SEM Micrographs acquired at different magnifications and Acquisition Times. *13th IMEKO TC15 Youth Symposium on Experimental Solid Mechanics 2014*. january 2014, p. 88–91.

[6] Goldstein, J., Newbury, D., Michael, J., Ritchie, N., Scott, J. et al. *Scanning Electron Microscopy and X-Ray Microanalysis*. January 2018. ISBN 978-1-4939-6674-5.

[7] Jones, H., Mingard, K. and Cox, D. Investigation of slice thickness and shape milled by a focused ion beam for three-dimensional reconstruction of microstructures. *Ultramicroscopy*. 2014, vol. 139, p. 20–28. DOI: https://doi.org/10.1016/j.ultramic.2014.01.003. ISSN 0304-3991. Available at: https://www.sciencedirect.com/science/article/pii/S0304399114000138.

[8] Principe, E. *High-density FIB-SEM tomography via real-time imaging*. 2010. US Patent US8178838B2.

[9] Kart, U., Lukežič, A., Kristan, M., Kämäräinen, J.-K. and Matas, J. Object Tracking by Reconstruction With View-Specific Discriminative Correlation Filters. In: *2019 IEEE/CVF Conference on Computer Vision and Pattern Recognition (CVPR)*. 2019, p. 1339–1348. DOI: 10.1109/CVPR.2019.00143.

[10] Bradski, G. The OpenCV Library. *Dr. Dobb's Journal of Software Tools*. 2000.

Appendix A

Contents of the included storage media

In this attachment, the contents of the storage media (DVD-R) are presented (see the schematic in Figure A.1).

Not all the files included are listed down below. For more detailed explanation of the storage media content, please, see the `readme.md` file in the root directory.

A brief description of the main files listed in Fig. A.1:

- `bin/CirclesDetection` – Folder containing the complete implementation of the algorithm for obtaining the ground truth (`.py` files).
- `bin/ImProcCV/HorizontalEdgeDetection.cs` – Implementation of the cut-face edge detection algorithm.
- `bin/SliceThicknessTopDownService.cs` – Implementation of the slice thickness measurement by both the Top-Down FIB and Y-Shift SEM.
- `bin/chevrons_detection.py` – Implementation of the Chevrons method.
- `data/Dataset1` – All images acquired for the Dataset 1, and parameters, which are needed for the measurement.
- `data/Dataset2` – All images acquired for the Dataset 2, and parameters, which are needed for the measurement.
- `data/Dataset3` – All images acquired for the Dataset 3, and parameters, which are needed for the measurement.
- `doc/...` – Master's thesis LaTeX source files.
- `Kutalek_Jiri_Measuring_the_thickness_of_material_layers_removed_from_a-sample_in_an_electron_microscope.pdf` – Master's thesis PDF file.
- `Kutalek_Jiri_poster.pdf` – The attached poster.
- `readme.md` – The main manual file with more detailed information about the the source files and the data stored on the media and recommendations for executing the individual scripts.

Figure A.1: Schematic of the storage media contents. More detailed information, including a description of all the files in the `bin` and `data` folders and the recommendations for the individual scripts, is in the `readme.md` file.